CALL FOR PAPERS: | *Computational Modeling of Physiological Systems*

Identifying physiological origins of baroreflex dysfunction in salt-sensitive hypertension in the Dahl SS rat

Scott M. Bugenhagen, Allen W. Cowley, Jr., and Daniel A. Beard

Department of Physiology, Medical College of Wisconsin, Milwaukee, Wisconsin

Bugenhagen SM, Cowley AW Jr, Beard DA. Identifying physiological origins of baroreflex dysfunction in salt-sensitive hypertension in the Dahl SS rat. *Physiol Genomics* 42: 23–41, 2010. First published March 30, 2010; doi:10.1152/physiolgenomics.00027.2010.—Salt-sensitive hypertension is known to be associated with dysfunction of the baroreflex control system in the Dahl salt-sensitive (SS) rat. However, neither the physiological mechanisms nor the genomic regions underlying the baroreflex dysfunction seen in this rat model are definitively known. Here, we have adopted a mathematical modeling approach to investigate the physiological and genetic origins of baroreflex dysfunction in the Dahl SS rat. We have developed a computational model of the overall baroreflex heart rate control system based on known physiological mechanisms to analyze telemetry-based blood pressure and heart rate data from two genetic strains of rat, the SS and consomic SS.13[BN], on low- and high-salt diets. With this approach, physiological parameters are estimated, unmeasured physiological variables related to the baroreflex control system are predicted, and differences in these quantities between the two strains of rat on low- and high-salt diets are detected. Specific findings include: a significant selective impairment in sympathetic gain with high-salt diet in SS rats and a protection from this impairment in SS.13[BN] rats, elevated sympathetic and parasympathetic offsets with high-salt diet in both strains, and an elevated sympathetic tone with high-salt diet in SS but not SS.13[BN] rats. In conclusion, we have associated several important physiological parameters of the baroreflex control system with chromosome 13 and have begun to identify possible physiological mechanisms underlying baroreflex impairment and hypertension in the Dahl SS rat that may be further explored in future experimental and modeling-based investigation.

computational model; baroreceptor reflex; autonomic nervous system

THE DAHL SALT-SENSITIVE (SS) rat is an extensively studied model of human salt-sensitive hypertension. Consomic substitution studies involving the introgression of whole chromosomes from a salt-resistant rat strain into the isogenic background of the SS strain, congenic substitution studies involving the introgression of smaller regions of chromosomes, and other genetic studies have led to the identification of many quantitative trait loci (QTLs) associated with this disease (12, 36, 44, http://www.pga.mcw.edu). However, phenotypes collected from many of these studies often involve relatively gross measurements such as blood pressure and heart rate, which provide little information on the underlying physiology. Many protective QTLs have been shown to interact epistatically (i.e., in a nonlinear or nonadditive manner) so that these measurements are unable to distinguish various combinations of introgressed QTLs (36). It is also likely that many QTLs have been left unidentified because of these interactions. Thus, these types of measurements become diminishingly informative with an increased degree of genetic nonlinearity.

It seems, then, that more detailed phenotypic measurements are required to understand the underlying etiology and to make sense of the genetics associated with this complex disease. Of course, this is not always possible; many measurements of interest are either inaccessible or simply not practical to obtain. In addition, many of these measurements are operating-point dependent and are influenced to a high degree by physiologic state. Methods of obtaining these measurements often require invasive techniques that introduce stressors (surgical, pharmacological, etc.) that may themselves alter physiological state and therefore the observed measurements. Thus, differences detected in such experimental measurements may not always indicate differences in underlying physiology but can rather indicate differences in confounding variables related to experimental conditions and/or methods.

Mechanistic mathematical models offer a powerful complement to laboratory measurements (5). By accounting for the dynamics of physiological control systems they can provide quantitative assessments of unmeasured variables and associated regulatory mechanisms under given experimental conditions. Here, we analyze high-level phenotype measurements using mathematical models to test hypotheses about the physiological mechanisms underlying differences in the baroreflex system between the SS and SS.13[BN] rat on high- and low-salt diets.

Baroreflex dysfunction is known to be associated with hypertension in human subjects (7) and has been associated with various rat models of hypertension including the Dahl SS rat and the spontaneously hypertensive (SHR) rat. Baroreflex dysfunction in the SHR model is characterized by both decreased pressure sensitivity (defined as the slope of the curve relating blood pressure to firing rate) and an increased pressure threshold (defined as the minimum blood pressure required for a response) of the afferent baroreceptor nerve fibers (8). It has been shown that this increased pressure threshold (i.e., baroreceptor resetting) is regulated by a mechanism (or mechanisms) independent of vessel distensibility (3). The gain in the overall baroreflex was shown to be blunted by a factor of about four in the SHR compared with the Wistar-Kyoto (WKY) strain (52), but studies of sympathetic baroreflex dysfunction in the SHR are conflicting (19, 52). Of greater interest to the present study are studies of baroreflex dysfunction in the SS rat. Similar to the SHR rat, afferent baroreceptor nerve fiber dysfunction in the SS rat is characterized by elevated pressure thresholds and reduced pressure sensitivity (4). A high-salt diet was shown to

Address for reprint requests and other correspondence: D. A. Beard, Dept. of Physiology, Medical College of Wisconsin, Milwaukee, WI 53226 (e-mail: dbeard@mcw.edu).

23

elevate pressure threshold but did not alter pressure sensitivity, in SS rats as well as in normal Dahl salt-resistant (SR) rats (2). Defects in both the sympathetic (33) and parasympathetic (61) baroreflex responses have been observed in SS rats on high-salt diets, but normal sympathetic baroreflex responses have been observed in rats on low-salt diets (20).

Kendziorski et al. (25) used a mathematical modeling approach to compare baroreflex function in the SS vs. Brown Norway (BN) rat and found a significant attenuation of baroreflex gain in the SS rat compared with the BN rat. Through linkage analysis, their study was able to map components of baroreflex function to chromosomes 4 and 10. In the present study, differences in baroreflex function between the SS rat strain and a consomic strain, the SS.13[BN], are characterized. The BN chromosome 13 has been shown to be associated with a marked reduction in blood-pressure salt sensitivity when introgressed into the SS genetic background (12, 36), but the physiological origins associated with its protective effects are yet to be fully understood. Because of the known associations of baroreflex dysfunction with hypertension along with the marked reduction in blood pressure salt sensitivity associated with the BN chromosome 13, the SS.13[BN] strain provides a useful control in the present study. Using this design, the goals are twofold: 1) to better characterize baroreflex dysfunction in the SS rat and 2) to identify any association of baroreflex heart rate control parameters with the chromosome 13.

MODEL DEVELOPMENT

The baroreflex is a nonlinear negative feedback control system known to be responsible for the reflex control of heart rate and believed to be involved in the short-term control of arterial blood pressure (11). Because this reflex plays such a fundamental role in cardiovascular physiology, it has been the subject of intensive investigation over the last several decades which has led to a much better understanding of the mechanisms underlying the various components of the reflex. There remains, however, much to be learned about both individual components and the overall operation of this control system. Most models describing the overall reflex are empirical in nature and ignore many of the known nonlinearities associated with the reflex. To dissect the origins of baroreflex dysfunction in the SS rat we have developed a model based on known physiological mechanisms associated with certain model components and parameterized using data available from the literature. Other model components are parameterized to match data from individual SS and SS.13[BN] rats on high- and low-salt diets to elucidate functional differences in the reflex system between these four groups. A block diagram of the model is shown in Fig. 1.

Afferent baroreceptor component. Afferent baroreceptor nerve fibers are strain sensors (21) found in both the aortic arch and the carotid sinus that respond to arterial blood pressure perturbations via changes in firing rate. Both myelinated and unmyelinated fibers are known to exist. Differences in both the static and dynamic characteristics of these two fiber types have been demonstrated (9, 57), but the significance of these differences is unknown. In addition, two general baroreceptor discharge patterns have been identified by Seagard et al. (50), which are summarized by the following characteristics: the type I pattern is characterized by a "discontinuous hyperbolic pattern" with relatively high threshold frequency and saturation firing rate whereas the type II pattern is characterized by a "continuous sigmoidal pattern" with a relatively low threshold frequency and saturation firing rate. Because the impact of fiber type differences in the overall reflex control of heart rate is not well characterized, we do not account for these differences in our model. Furthermore, blood pressure data collected for this study come from aorta only, and we therefore ignore contributions from the carotid sinus baroreceptors. This is not expected to present any major shortcomings given that baroreceptors of the aortic arch have recently been shown to play a dominant role in the baroreflex control of heart rate (42).

The nonlinear features of the baroreceptor response include threshold, saturation, asymmetry, and adaptation. Several basic approaches have been used to capture these important features [see review by Taher et al. (56)]. While the biophysical origins of these nonlinearities are not completely characterized, it is clear that viscoelastic processes of the baroreceptor nerve endings contribute (16). In this study, the modeling approach of Srinivasan et al. (54, 55) is adopted, incorporating refinements proposed by Alfrey (1). The Srinivasan model is based on known mechanisms underlying mechanoreception and divides the afferent baroreceptor into aortic wall, nerve ending, transducer, and encoder components. The aortic wall model used by Srinivasan et al. is based on a complicated pressure-volume relationship derived for cylindrical tubes with elastomeric walls (26). As an alternative to their model, we may represent the static aortic wall using a three-parameter empirical pressure-area relationship proposed by Langewouters et al. (27):

$$A = A_m \left\{ \frac{1}{2} + \frac{1}{\pi} \tan^{-1} \left(\frac{P - P_0}{P_1} \right) \right\}, \qquad (1)$$

where A is the aorta cross-sectional area, A_m is the maximal cross-sectional area, P_o is the aortic pressure at which the compliance curve reaches a maximum, and P_1 represents the steepness of rise, or compliance, of the curve and is called the half-width pressure. This function is used to fit an average
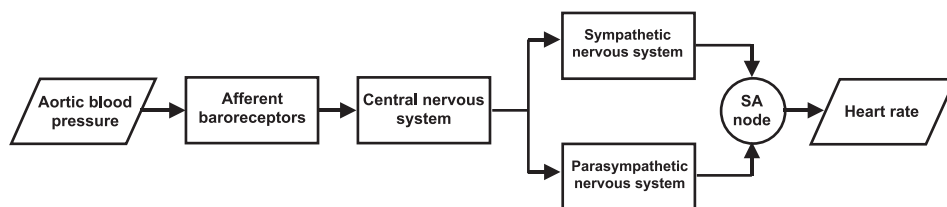

Fig. 1. Overall baroreflex flow diagram. The various subcomponents comprising the model of the overall baroreflex control of heart rate are shown. Aortic blood pressure serves as the model input and is transduced to a neural signal (firing rate) by afferent baroreceptors found in the aortic arch. This neural signal is further processed by the central nervous system (CNS). The output of the CNS serves to modulate the activities (outflows) of the 2 parallel pathways of the peripheral nervous system (sympathetic and parasympathetic). These 2 pathways exert reciprocal effects at the sinoatrial (SA) node of the heart, which is the ultimate effector of heart rate. Heart rate is the final output of the model.
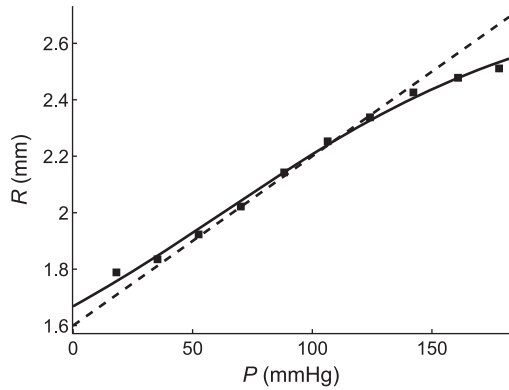
Fig. 2. Pressure-radius relationship of rat aorta. The radius (R) of the aorta is plotted against transmural pressure (P) in the aorta. Data (■) are from Andresen (3) and represent the average external radii of a group of aortas excised from SHR rats at the given transmural pressures. The 2 lines shown represent fits to data of 2 versions of our static aortic wall model. The solid line represents fits of the 3-parameter nonlinear model given by *Eq. 1* with $A_m =$ 28.76 mm², $P_o = 87.52$ mmHg, and $P_1 = 123.76$ mmHg. The dotted line represents the linearized 2-parameter model given by *Eq. 4* with $R_o = 1.6$ mm and $C_{wall} = 0.006$ mm/mmHg. With the exception of the high-pressure region, the linear model approximates the pressure-radius relationship as well as the nonlinear model.

pressure-radius curve from a group of SHR rats obtained from data of Andresen (3) and plotted in Fig. 2. Fits of *Eq. 1* to the data in Fig. 2, plotted as a solid line in the figure, yield parameter estimates $P_o = 87.52$ mmHg, $P_1 = 123.76$ mmHg, and $A_m = 28.76$ mm². (Radius R and area A are related by $R = \sqrt{A/\pi}$.)

Following Srinivasan et al. (54, 55), the static expression of *Eq. 1* can be used to generate a dynamic model:

$$\frac{dA}{dt} = \frac{-P_1 \tan\left\{\pi\left(\frac{A}{A_m} - \frac{1}{2}\right)\right\} - P_0 + P}{B_{wall}}, \quad (2)$$

where B_{wall} represents the viscosity associated with the aortic wall. Aortic wall strain, ε_{wall}, can be computed from aortic radius R according to

$$\varepsilon_{wall} = \frac{R - R_0}{R_0} \quad (3)$$

where R_o is the unstressed radius of the aorta.

Since, over the pressure ranges of interest, the pressure-radius curve shown in Fig. 2 is approximately linear, we chose to simplify the aortic wall component by modeling the pressure-area relationship as

$$A = \pi\left(R_0 + C_{wall}P\right)^2 \quad (4)$$

where C_{wall} represents the slope of the pressure-radius curve. The dynamic wall model then becomes

$$\frac{dA}{dt} = \frac{-\dfrac{\sqrt{A/\pi} - R_0}{C_{wall}} + P}{B_{wall}}. \quad (5)$$

The fit to this simple linear model is shown as a dashed line in Fig. 2, for parameter values $R_o = 1.6$ mm and $C_{wall} = 0.006$ mm/mmHg.

In the Srinivasan model, the aortic wall strain and dynamic strain associated with friction at the nerve ending are uncoupled, and a separate parameter is varied as a function of static input pressure to achieve fits to a variety of data. A more physiological model of baroreceptor nerve-aortic wall coupling based on models of muscle spindles is proposed by Alfrey (1). This model includes a rapid adaptation phase modeled by a single Voigt body and a slower adaptation phase, also known as the rapid resetting phase, modeled by a single dashpot that was allowed to completely reset. However, Brown et al. (8) found that 90% of baroreceptor adaptation to pressure steps occurred within 2–3 s after the maximum firing frequency and that a steady-state level was reached in ∼10–20 s. This suggests that two time constants (and therefore two Voigt bodies) would better account for the rapid adaptation phase. In addition, Munch et al. (38) found that the extent of rapid resetting averaged only 33% and had a time constant of 180–250 s. Thus, the dashpot model of rapid resetting in the Alfrey model (which resets 100%) would be better represented with an additional Voigt body since complete resetting does not occur in the rapid resetting phase. Our proposed model of baroreceptor coupling dynamics is illustrated in Fig. 3 and is described by the following system of ordinary differential equations:
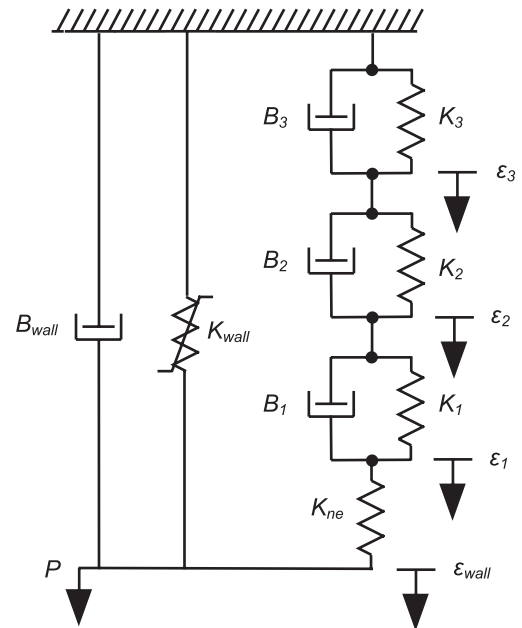

Fig. 3. Dynamic baroreceptor mechanics model. Aortic wall mechanics and coupling of the baroreceptor nerve ending to the aortic wall and surrounding connective tissue are modeled by the spring and dashpot system shown. The nonlinear spring, K_{wall}, and dashpot, B_{wall}, represent the elasticity and viscosity of the aortic wall, respectively. The spring K_{ne} represents the elasticity of the baroreceptor nerve ending. The 3 Voigt bodies (modeled by parallel spring and dashpot units) represent the viscoelastic properties of the connective tissues surrounding the baroreceptor nerve ending. The model responds to aortic pressure (P) perturbations via changes in strain (ε) across the various subcomponents. The baroreceptors respond to the strain sensed across the baroreceptor nerve ending, δ, equal to $\varepsilon_{wall} - \varepsilon_1$.

$$\frac{d\varepsilon_1}{dt} = \frac{K_{ne}(\varepsilon_{wall} - \varepsilon_1) - K_1(\varepsilon_1 - \varepsilon_2)}{B_1} + \frac{d\varepsilon_2}{dt}$$

$$\frac{d\varepsilon_2}{dt} = \frac{K_1(\varepsilon_1 - \varepsilon_2) - K_2(\varepsilon_2 - \varepsilon_3) + B_1\dfrac{d\varepsilon_1}{dt} + B_2\dfrac{d\varepsilon_3}{dt}}{B_1 + B_2}$$

$$\frac{d\varepsilon_3}{dt} = \frac{K_2(\varepsilon_2 - \varepsilon_3) - K_3\varepsilon_3 + B_2\dfrac{d\varepsilon_2}{dt}}{B_2 + B_3}$$

$$(6)$$

where the εs are strains, the Ks are elastic constants, and the Bs are viscous constants. The subscript ne denotes nerve ending, and subscripts *1*, *2*, and *3* denote various components of the surrounding connective tissue. The strain dynamics governed by *Eq. 6* are driven by the wall strain, ε_{wall}, which changes in response to changes in pressure according to *Eqs. 4* and *5*. The strain sensed by the baroreceptor nerve ending is given by

$$\delta = \varepsilon_{wall} - \varepsilon_1. \qquad (7)$$

In the Srinivasan model, the baroreceptor threshold and "jump frequency" phenomena are accounted for in the transduction component and are modeled by a set of empirical functions. The encoder model consists of a simple integrate-and-fire mechanism. We have adapted a simpler form of the Srinivasan transducer and encoder components given by the equation below:

$$n = \begin{cases} 0, & \text{if } \delta < \delta_{th} \\ S(\delta - \zeta\delta_{th}), & \text{if } \delta \geq \delta_{th} \end{cases}. \qquad (8)$$

Here n represents afferent baroreceptor firing rate, S represents baroreceptor strain sensitivity, δ_{th} represents strain threshold, and ζ is a parameter introduced to account for the jump frequency at threshold. The parameter ζ is dimensionless with its value constrained between 0 and 1.

Because of the wealth of dynamic baroreceptor response data from the WKY rat available in the literature, we have parameterized a generic (rat strain-independent) model of afferent baroreceptor dynamics using pressure step-response data from this strain. That is, we treat parameters from this component of the model as constants when we analyze data from other rats. This seems reasonable given that Brown et al. (8, 9) were unable to identify any differences in the dynamic baroreceptor response in normotensive WKY rats vs. hypertensive SHR rats. We assume this holds true in the Dahl SS and related consomic strains as well. Model fits to step-response data from Brown et al. (8) and ramp-response data from Andresen (3) are shown in Fig. 4 with associated parameter estimates provided in the legend.

On the other hand, baroreceptor static response parameters, including pressure/strain sensitivity and threshold, have been
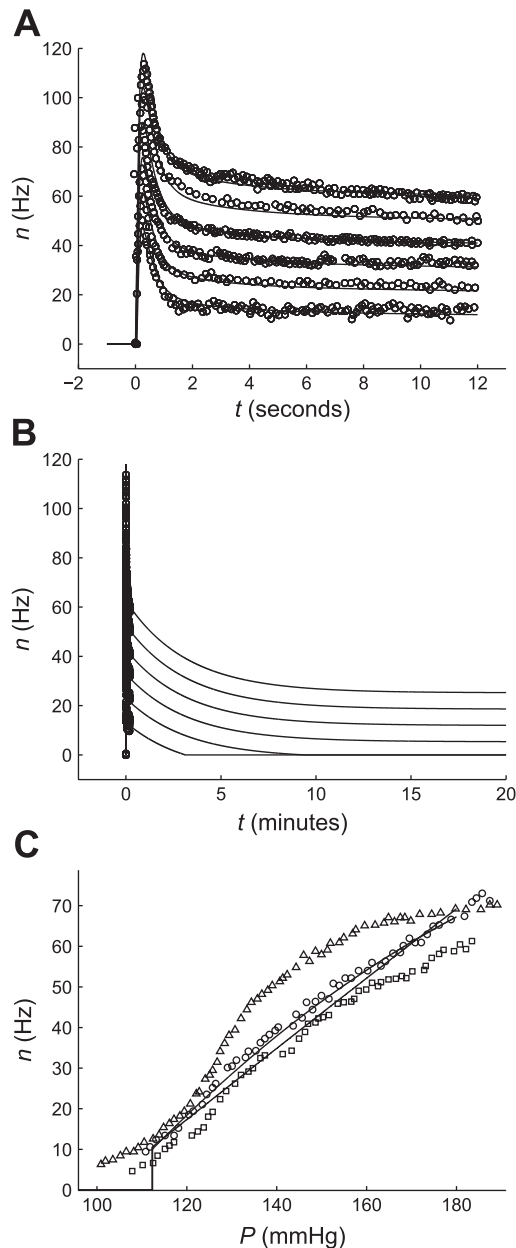
Fig. 4. Afferent baroreceptor model fits. The afferent baroreceptor model, given by *Eqs. 1–9*, is used to fit step (*A*) and ramp (*C*) datasets associated with the WKY rat strain. *A*: dynamic components of the model are parameterized using baroreceptor step-response data (○) collected in experiments of Brown et al. (8). Pressure steps of 130 (*bottom* trace), 150, 170, 190, 210, and 230 (*top* trace) mmHg were applied to an isolated aortic arch preparation. The linearized version of the dynamic model (*Eq. 5*) was used to produce the fits (solid lines) shown. The optimal values of the dynamic parameters estimated from these fits are $K_{ne} = 1$, $K_1 = 1.5$, $K_2 = 3.75$, $K_3 = 1.05$, $B_1 = 1$, $B_2 = 10$, $B_3 = 300$, $B_{wall} = 1$ (note: units of Ks are mmHg/mm and units of Bs are mmHg·s/mm). The values of static parameters used to produce these fits are $S = 255$ Hz, $\delta_{th} = 0.2$, and $\zeta = 1$. *B*: model fits to *A* are illustrated in a time-scale consistent with the rapid-resetting phase of the response. There were not sufficient data in the 12 second step-response data of Brown et al. to identify the model components associated with the rapid-resetting phase. Therefore, the parameter B_3 in our model was not identified here. *C*: model fits to 2 mmHg/s pressure ramp-response data (open markers) of a population of 3 baroreceptor fibers collected in experiments of Andresen (3) are shown. Both the nonlinear (solid line) and linearized (dashed line) models were used to fit the data associated with the circle markers. The values of static parameters used to produce the nonlinear fit are $S = 800$ Hz, $\delta_{th} = 0.18$, and $\zeta = 0.93$. The values used to produce the linear fit are $S = 500$ Hz, $\delta_{th} = 0.21$, and $\zeta = 0.9$. The values of dynamic parameters used in the fits of *C* are the same as those used to produce the fits of *A*. The values of the static parameters used to produce the fits of *C* were not used in later analyses. Instead, values of these static parameters were selected to match data of the SS strain (from Ref. 4, not shown) and are given in Table 1.

shown to be quite different between rat strains (2–4). In the present study, we are interested in differences in baroreflex sensitivities and thresholds between the rat strains studied. However, the afferent baroreceptors are not the only components contributing to the sensitivity and threshold properties of the overall baroreflex, and the heart rate data used to parameterize the overall model cannot inform the model of the relative contributions of the various subcomponents to these system properties. We therefore parameterize the sensitivity parameter S of our afferent baroreceptor model using ramp-data available for the SS rat (4) and set the threshold δ_{th} to zero. (Threshold is instead accounted for in the peripheral nervous system component of our model.) The full set of parameter values used in the afferent baroreceptor model is listed in Table 1.

Central and peripheral nervous system components. The least well-understood component of the baroreflex control of heart rate is the integration of baroreceptor afferent signals at the nucleus tractus solitarius (NTS) in the medulla of the brain stem. Important aspects of NTS integration have only recently been discovered. For example, the NTS is now known to be sensitive to many characteristics of the input signal (46, 47), and NTS network architecture is thought to play an important role in determining its response patterns (45). In addition, higher brain centers are thought to play a modulatory role in the integration of sensory signals at the NTS (51, 53, 60) and are thought to continuously modulate baroreflex gain to "optimize the response of the cardiovascular system to daily life challenges" (13, 14). Because of these many complexities, most existing models of the central component of the baroreflex are empirical in nature, many of which are derived through transfer function analysis. These models usually lump the central and peripheral nervous system components together. For instance, Petiot et al. (41) modeled the frequency response of sympathetic nervous activity to aortic depressor nerve stimulation in rat using derivative gain in combination with an overdamped second-order low-pass filter. Their analysis was limited to the linear range of the sympathetic response. Likewise, Kawada et al. (23, 24) successfully modeled the dynamic sympathetic nervous system regulation by the arterial baroreflex using derivative and second order low-pass filters followed by a sigmoidal nonlinearity in rabbit.

For simplicity, we model the central component as an all-pass filter given by

$$\alpha_{cns} = G_{cns}n \qquad (9)$$

where α_{cns} is central nervous system activity and G_{cns} is central gain. Here, G_{cns} is set to 1. The peripheral nervous system is modeled by two parallel sigmoidal nonlinearities (one for the sympathetic pathway and the other for the parasympathetic pathway) given by the following 4-parameter logistic functions:

$$T_s = T_{s,\min} + \frac{T_{s,\max} - T_{s,\min}}{e^{G_s(\alpha_{cns}-\alpha_{s,o})} + 1}$$
$$T_p = T_{p,\min} + \frac{T_{p,\max} - T_{p,\min}}{e^{-G_p(\alpha_{cns}-\alpha_{p,o})} + 1} \qquad (10)$$

where T_s and T_p represent sympathetic and parasympathetic tones, $T_{s,min}$ and $T_{p,min}$ represent minimum tones, $T_{s,max}$ and $T_{p,max}$ represent maximum tones, and G_s and G_p represent sympathetic and parasympathetic gains, respectively. Here, gain is defined as the steepness of the sympathetic and parasympathetic sigmoidal tone curves. Note that this definition is in contrast to the more standard definition of gain, which is the ratio of the magnitude of an output signal to an input signal (49). Unlike the ratios of the magnitudes of T_s and T_p to α_{cns},

Table 1. *Afferent baroreceptor model parameters and variables*

Name	Definition	Value	Units
Variables			
P	aortic blood pressure		mmHg
A	aortic cross-sectional area		mm^2
R	aortic radius		mm
ε_{wall}	aortic wall strain		unitless
ε_1	baroreceptor connective tissue strain		unitless
ε_2	baroreceptor connective tissue strain		unitless
ε_3	baroreceptor connective tissue strain		unitless
δ	baroreceptor nerve ending strain		unitless
n	baroreceptor firing rate		Hz
Parameters			
S	strain sensitivity	480	Hz
δ_{th}	strain threshold	0	unitless
ζ	threshold firing frequency scaling factor	1	unitless
R_o	aortic unstressed radius	1.6	mm
C_{wall}	aortic distensibility constant	0.006	mm/mmHg
K_{ne}	baroreceptor nerve ending elastic constant	1	mmHg/mm
K_1	baroreceptor connective tissue elastic constant	1.5	mmHg/mm
K_2	baroreceptor connective tissue elastic constant	3.75	mmHg/mm
K_3	baroreceptor connective tissue elastic constant	1.05	mmHg/mm
B_{wall}	aortic wall viscous constant	1	mmHg $\times$ s/mm
B_1	baroreceptor connective tissue viscous constant	1	mmHg $\times$ s/mm
B_2	baroreceptor connective tissue viscous constant	10	mmHg $\times$ s/mm
B_3	baroreceptor connective tissue viscous constant	adjustable	mmHg $\times$ s/mm

Parameter and variable names, definitions, and units associated with the afferent baroreceptor component of the model are listed. Parameter values used to analyze data from SS and SS.13[BN] rats on high- and low-salt diets are given. Parameter values designated as "adjustable" are estimated from experimental data on individual rats from the 4 groups. The optimal values of these adjustable parameters are given in Table 5.

G_s and G_p are operating point independent. The parameters $\alpha_{s,o}$ and $\alpha_{p,o}$ represent baseline or offset sympathetic and parasympathetic activity (defined as horizontal shifts in the sympathetic and parasympathetic sigmoidal tone curves of *Eq. 10*), respectively, and account for the "central threshold" described by Eckberg (15). A similar approach has been used in previous studies (30, 32).

Since we set the baroreflex strain sensitivity S to a constant value and we model the central component as an all-pass filter, the sensitivities to change in pressure are lumped into the gain parameters, G_s and G_p. We allow G_s and G_p to vary independently so that selective differences in the sympathetic and parasympathetic limbs may be detected. Similarly, because baroreceptor threshold is ignored and assumed to be accounted for by higher level components in the model, $\alpha_{s,o}$ and $\alpha_{p,o}$ are interpreted as representing thresholds. Similar to the gains, we allow these offset parameters to be varied independently. Because the parasympathetic limb has been shown to operate at a higher pressure than the sympathetic limb (17, 52), we constrain $\alpha_{p,o}$ to be greater than $\alpha_{s,o}$. The parameters involved in our central and peripheral nervous system components are summarized in Table 2.

Effector component. The baroreflexes exert their chronotropic effects through the reciprocal action of the neurotransmitters norepinephrine and acetylcholine on the sinoatrial node of the heart. Norepinephrine is released from the cardiac sympathetic nerve and acts to accelerate heart rate, whereas acetylcholine is released from the vagus nerve and acts to decelerate heart rate. The secretion rates of norepinephrine and acetylcholine depend on sympathetic and parasympathetic stimulation frequencies, respectively, which are modulated by the baroreflexes via the mechanisms described above. Parasympathetic stimulation is known to exert beat-by-beat control of heart rate, whereas sympathetic control of heart rate is a more gradual process that is unable to exert beat-by-beat control (28, 34, 35).

Mokrane and Nadeau (35) studied the dynamics of the sympathetic heart rate response in dog using a cardiac sympa-

thetic nerve electrical stimulation protocol and developed a model that successfully simulated the dynamic heart rate response to sympathetic stimulation. We assume that sympathetic heart rate dynamics in dog match those in rat and have adapted the Mokrane model in our analysis. Release of norepinephrine from the cardiac sympathetic nerve is given by

$$\frac{dc_{nor}}{dt} = -\frac{c_{nor}}{\tau_{nor}} + q_{nor}T_s \qquad (11)$$

where c_{nor} is proportional to norepinephrine concentration at the sinus node, T_s is sympathetic tone, q_{nor} is the norepinephrine secretion rate constant, and τ_{nor} is the time constant of norepinephrine reuptake processes. The value of $\tau_{nor} = 9.1$ s used in our model is taken from Mokrane and Nadeau (35). Levy et al. (28) demonstrated that the secretion rate of norepinephrine is proportional to the rate of reuptake; q_{nor} was therefore assigned the value τ_{nor}^{-1}. Sympathetic tone is measured in this model in arbitrary units (AU). Therefore, the variable c_{nor} is measured in arbitrary units as well. (It is possible but not necessary to introduce an additional arbitrary conversion factor to express c_{nor} in concentration units.)

The heart rate response to sympathetic stimulation is known to saturate in the physiological range (6). As in the Mokrane-Nadeau model, this saturation effect is accounted for in the static response of the heart to sympathetic stimulation ($\Delta HR_{s,s}$), and is modeled by the Hill equation with a Hill coefficient of 2:

$$\Delta HR_{s,s} = \frac{\Delta HR_{s,\max}c_{nor}^2}{K_{nor}^2 + c_{nor}^2}. \qquad (12)$$

K_{nor} is the level of norepinephrine producing a half-maximal response, and $\Delta HR_{s,max}$ is the maximum increase in heart rate due to sympathetic stimulation:

$$\Delta HR_{s,\max} = HR_{\max} - HR_o \qquad (13)$$

where HR_{max} is the maximum heart rate and HR_o is the intrinsic heart rate. The dynamic response of the change in heart rate due to sympathetic stimulation is modeled by the first order process given below

$$\frac{d\Delta HR_s}{dt} = \frac{-\Delta HR_s + \Delta HR_{s,s}}{\tau_{HR,nor}} \qquad (14)$$

where ΔHR_s is the dynamic increase in heart rate due to sympathetic stimulation and $\tau_{HR,nor}$ is the time constant associated with sympathetic heart rate dynamics. The value $\tau_{HR,nor} = 2.1$ s is taken from Mokrane and Nadeau (35). The value of $K_{nor} = 1.12$ AU is estimated using dynamic sympathetic heart rate response data from Warner and Cox (58) as shown in Fig. 5. The values of HR_o and HR_{max} are adjusted to match data from individual rats in the overall model.

In our model, the parasympathetic heart rate response assumes the same form as the sympathetic heart rate response model described above:

$$\frac{dc_{ach}}{dt} = -\frac{c_{ach}}{\tau_{ach}} + q_{ach}T_p \qquad (15)$$

where c_{ach} is proportional to the concentration of acetylcholine at the sinus node, T_p is parasympathetic tone, q_{ach} is the

Table 2. *Central/peripheral nervous system model parameters and variables*

Name	Definition	Value	Units
Variables			
α_{cns}	central nervous system activity		Hz
T_s	sympathetic tone		AU
T_p	parasympathetic tone		AU
Parameters			
G_{cns}	central gain	1	unitless
G_s	sympathetic gain	adjustable	Hz^{-1}
G_p	parasympathetic gain	adjustable	Hz^{-1}
$T_{s,max}$	maximum sympathetic tone	adjustable	AU
$T_{p,max}$	maximum parasympathetic tone	adjustable	AU
$T_{s,min}$	minimum sympathetic tone	adjustable	AU
$T_{p,min}$	minimum parasympathetic tone	adjustable	AU
$\alpha_{s,o}$	sympathetic offset	adjustable	Hz
$\alpha_{p,o}$	parasympathetic offset	adjustable	Hz

Parameter and variable names, definitions, and units associated with the CNS and PNS components of the model are listed. Parameter values used to analyze data from SS and SS.13[BN] rats on high- and low-salt diets are given. Parameter values designated as "adjustable" are estimated from experimental data on individual rats from the 4 groups. The optimal values of these adjustable parameters are given in Table 5.
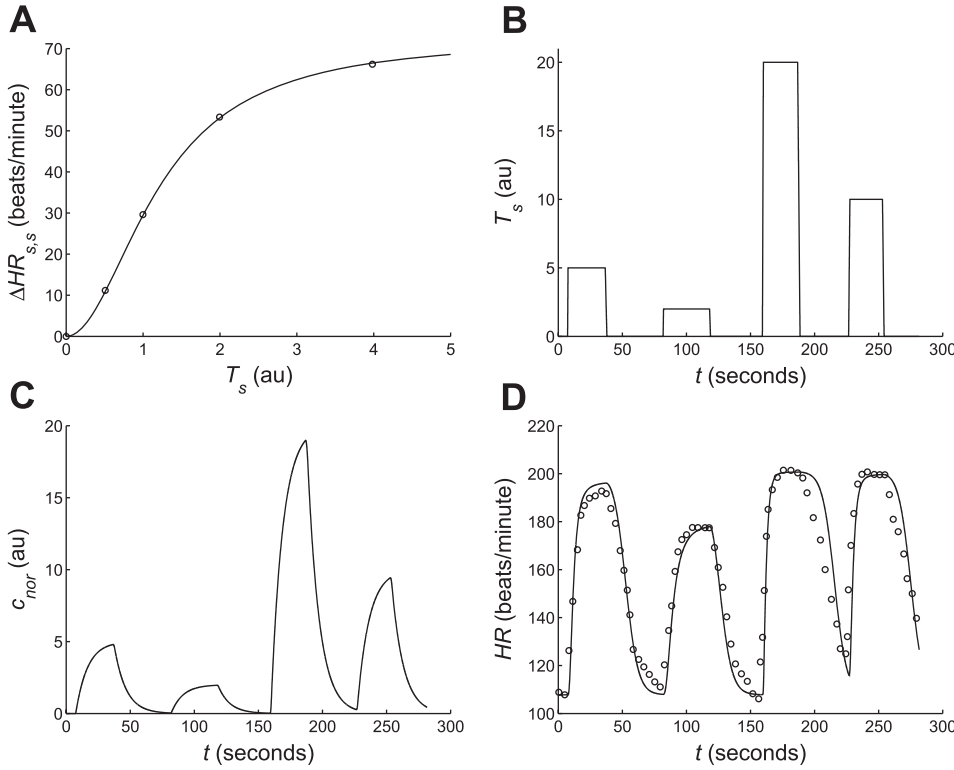
Fig. 5. Modeling the sympathetic control of heart rate. *A*: the static heart rate response to sympathetic stimulation ($\Delta HR_{s,s}$) is plotted against cardiac sympathetic nerve stimulation frequency (T_s). Data (○) and model fit (solid line) are reproduced from Mokrane and Nadeau (35) demonstrating the saturation of the static heart rate response to increasing sympathetic stimulation frequency, which can be modeled using *Eq. 12*. *B–D*: the sympathetic heart rate model, given by *Eqs. 11–14*, is used to fit dynamic sympathetic heart rate response data collected in experiments of Warner and Cox (58). In the experiments, the pulse stimuli shown in *B* were applied to the cut end of the cardiac sympathetic nerve which produced corresponding changes in heart rate (*HR*) as shown in *D*. Using these pulse stimuli as an input, the model (solid lines) was fit to the heart rate data (○) of *D* by adjusting the values of the parameters HR_o, HR_{max}, and K_{nor}. Optimal values for the fits shown are $HR_o = 107.8$ beats/min, $HR_{max} = 201$ beats/min, and $K_{nor} = 1.12$ AU. Values of time constants were held constant. The model predicted (unmeasured) concentration of norepinephrine (c_{nor}) at the sinoatrial node is shown in *C*.

acetylcholine secretion rate, and τ_{ach} is the time constant associated with acetylcholine hydrolysis. The value of $\tau_{ach} = 0.2$ s used in our model is taken from Levy et al. (28). As in the sympathetic heart rate model, q_{ach} is assigned the value τ_{ach}^{-1}. Parasympathetic tone T_P and the variable c_{ach} are measured in this model in AU.

There is a known relationship between heart rate variability (HRV) and parasympathetic activity that has been described as "a function in which there is an ascending limb where HRV increases as parasympathetic effect increases until it reaches a plateau level; HRV then decreases as parasympathetic effect increases" (18). This suggests that, like the sympathetic heart rate response, the parasympathetic heart rate response saturates in the physiological range. Using data from Warner and Cox (58) (Fig. 6*A*), we found that a function of identical form to *Eq. 12* may be used to characterize the static heart rate response to parasympathetic stimulation:

$$\Delta HR_{p,s} = \frac{\Delta HR_{p,max} c_{ach}^2}{K_{ach}^2 + c_{ach}^2}. \qquad (16)$$

Here, K_{ach} is the level of acetylcholine producing a half-maximal response, and $\Delta HR_{p,max}$ is the maximum decrease in heart rate due to parasympathetic stimulation, and is given by

$$\Delta HR_{p,max} = HR_o - HR_{min} \qquad (17)$$

where HR_{min} is the minimum heart rate and HR_o is the intrinsic heart rate.

Mokrane et al. (34) used a transfer function to characterize the dynamic heart rate response to vagal stimulation. The vagal heart rate response was characterized by a combination of two different filter behaviors: a low-pass filter with a mean time constant of 2.5 s and an all-pass filter. These two filter behaviors are likely due to acetylcholine acting through both a fast G protein-coupled pathway as well as a slower second-messenger pathway (28). We account for these two filter behaviors using an algebraic and a first order differential equation:

$$\Delta HR_{p,fast} = \gamma \Delta HR_{p,s}$$
$$\frac{d\Delta HR_{p,slow}}{dt} = \frac{-\Delta HR_{p,slow} + (1 - \gamma)\Delta HR_{p,s}}{\tau_{HR,ach}} \qquad (18)$$

where $\Delta HR_{p,fast}$ and $\Delta HR_{p,slow}$ represent the parasympathetic mediated decreases in heart rate due to fast and slow pathways, γ is the proportion of the dynamic response acting through the fast pathway, and $\tau_{HR,ach}$ is the time constant associated with the slow pathway (assigned the value 2.5 s). The overall parasympathetic heart rate response, then, is given by the sum of the individual fast and slow pathways as shown below:

$$\Delta HR_p = \Delta HR_{p,fast} + \Delta HR_{p,slow}. \qquad (19)$$

The time-dependent response of *HR* (from Ref. 58) to the dynamic parasympathetic stimulation protocol shown in Fig. 6*B* allows us to estimate values for K_{ach} and γ of 0.65 AU and 0.75, respectively. Values for the parameters HR_o and HR_{min} are obtained on an individual basis from experiments in the present study.

It has long been known that combined sympathetic and parasympathetic stimulation does not produce an algebraically additive effect at the sinoatrial node. Combined autonomic effects are instead complicated by an interaction between the two pathways (29). Rosenblueth and Simeone (48) accounted for this interaction using a model that multiplied two factors, one for each autonomic pathway, concluding that the sympa-
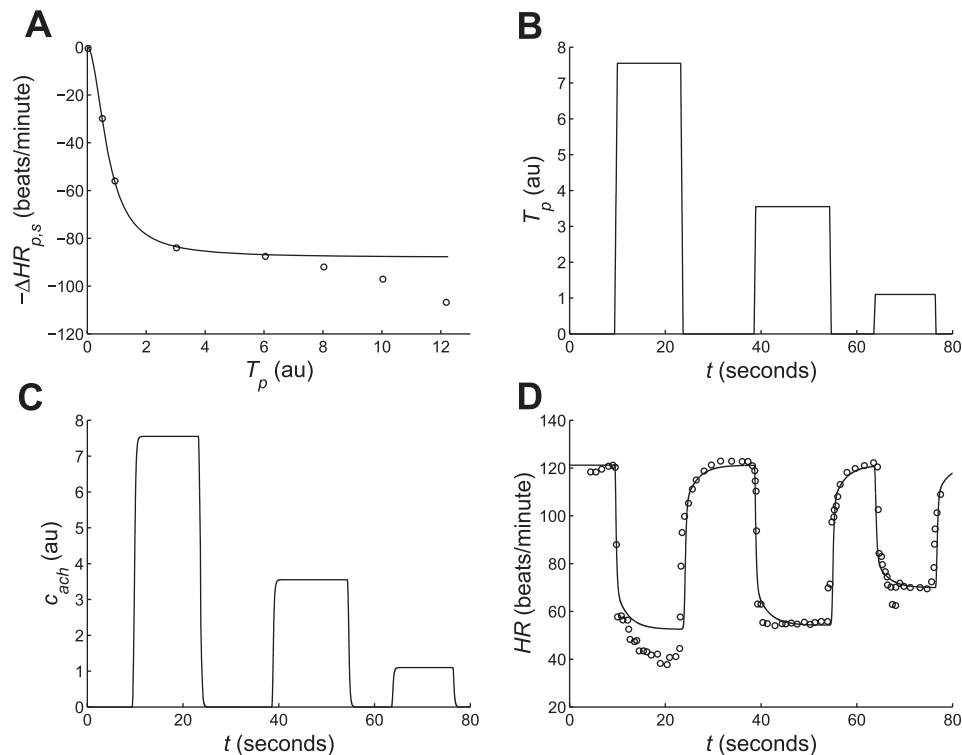
Fig. 6. Modeling the parasympathetic control of heart rate. *A*: the static heart rate response to parasympathetic stimulation ($\Delta HR_{p,s}$) was measured in an experiment by Warner and Cox (58) involving the electrical stimulation of the cut end of the vagus nerve (T_p) innervating the heart of a mongrel dog. Static heart rate response data from the experiment (○) is modeled using Equation (16) (solid line). The model cannot account for the inflection of the data occurring at ∼6 AU vagal stimulation. It is unknown whether this inflection occurs with normal physiological stimulation. *B–D*: the parasympathetic heart model, given by *Eqs. 15–19*, is used to fit dynamic parasympathetic heart rate response data collected in experiments of Warner and Cox (58). In the experiments, the pulse stimuli shown in *B* were applied to the cut end of the vagus nerve, which produced corresponding changes in heart rate as shown in *D*. Using these pulse stimuli as an input, the model (solid lines) was fit to the heart rate data (○) of *D* by adjusting the values of the parameters HR_o, HR_{min}, K_{ach}, and γ. Optimal values for the fits shown are HR_o = 121 beats/min, HR_{min} = 52 beats/min, K_{ach} = 0.65 AU, and γ = 0.75. Values of time constants were held constant. The model slightly underestimates the heart rate response to the strongest applied stimulus (≈7.5 AU). This is consistent with the inability of the static heart rate response model to account for the inflection seen in the data of *A* in this range of stimulus intensity. Therefore, the maximum value of T_p was constrained to a value below which this point of inflection occurs. The model-predicted (unmeasured) level of acetylcholine (c_{ach}) at the sinoatrial node is shown in *C*.

thetic and parasympathetic pathways exerted their effects independently of one another. Warner and Russell (59) proposed a different model, dismissed the findings of Rosenblueth and Simeone, and determined that the two pathways do indeed interact. Katona et al. (22) later recognized that the two models were essentially the same and that the different conclusions drawn from the models were a matter of interpretation. Here, we adapt the model of Warner and Russell to account for the combined sympathetic and parasympathetic effects on heart rate:

$$HR = HR_p + \frac{(HR_s - HR_o)(HR_p - \beta HR_{min})}{(HR_o - \beta HR_{min})} \quad (20)$$

where HR_s and HR_p are given by

$$\begin{aligned} HR_s &= HR_o + \Delta HR_s \\ HR_p &= HR_o - \Delta HR_p \end{aligned} \quad (21)$$

In our model, β is an adjustable parameter constrained between 0 and 1.

Parameters used in our heart rate effector component are summarized in Table 3. Values of fixed parameters are indicated in the table. Parameters identified as adjustable are estimated on an individual basis in the analysis below. Yet, before individual data are analyzed, the heart rate effector

model may be validated based on independent data from Warner and Russell (59). Figure 7*A* shows a dynamic stimulation protocol combining vagal and sympathetic stimulation. The associated measured and model-predicted heart rate data are shown in Fig. 7*B*. These model predictions, which involve no additional parameter adjustments (besides the adjustable parameters β, HR_o, HR_{max}, and HR_{min}), demonstrate that the model is able to accurately simulate the major features of the heart rate response to combined stimulation.

METHODS

Generation of consomic population. The consomic rat line was derived from inbred normotensive BN/SsNHsd/Mcw (BN) rats and salt-sensitive hypertensive Dahl SS/JrHsdMcwi (SS) in which the chromosome 13 of the BN was introgressed into the background of the SS as we have described previously (12).

Chronic phenotyping protocol. Blood pressure was measured by radiotelemetry using a Dataquest ART 3.1 system (Data Sciences International; DSI, St. Paul, MN). A gel-filled catheter connected to a transmitter (model TA11PA-C40, DSI) was surgically implanted in the femoral artery with the transmitter anchored under the skin over the flank area of the rat. Rats used were adult, male and female of the SS or the consomic SS.13^{BN} strain obtained from in-house colonies. These animals were maintained from weaning on a custom AIN-76

Table 3. *Heart rate effector model parameters and variables*

Name	Definition	Value	Units
Variables			
c_{nor}	norepinephrine concentration		AU
c_{ach}	acetylcholine concentration		AU
$\Delta HR_{s,s}$	static sympathetic heart rate response		beats/min
$\Delta HR_{p,s}$	static parasympathetic heart rate response		beats/min
ΔHR_s	sympathetic heart rate response		beats/min
$\Delta HR_{p,fast}$	parasympathetic heart rate response of fast pathway		beats/min
$\Delta HR_{p,slow}$	parasympathetic heart rate response of slow pathway		beats/min
ΔHR_p	overall parasympathetic heart rate response		beats/min
HR_s	sympathetic heart rate effect		beats/min
HR_p	parasympathetic heart rate effect		beats/min
HR	heart rate		beats/min
Parameters			
τ_{nor}	norepinephrine reuptake time constant	9.1	seconds
τ_{ach}	acetylcholine hydrolysis time constant	0.2	seconds
q_{nor}	norepinephrine secretion rate constant	0.1099	seconds^{-1}
q_{ach}	acetylcholine secretion rate constant	5	seconds^{-1}
K_{nor}	norepinephrine half-activation concentration	1.12	AU
K_{ach}	acetylcholine half-activation concentration	0.65	AU
$\Delta HR_{s,max}$	maximum sympathetic heart rate response	adjustable	beats/min
$\Delta HR_{p,max}$	maximum parasympathetic heart rate response	adjustable	beats/min
$\tau_{HR,nor}$	norepinephrine heart rate response time constant	2.1	seconds
$\tau_{HR,ach}$	slow acetylcholine heart rate response time constant	2.5	seconds
γ	fast pathway proportion	0.75	unitless
HR_{max}	maximum heart rate	adjustable	beats/min
HR_{min}	minimum heart rate	adjustable	beats/min
HR_o	intrinsic heart rate	adjustable	beats/min
β	interaction constant	adjustable	unitless

Parameter and variable names, definitions, and units associated with the heart rate effector components of the model are listed. Parameter values used to analyze data from SS and SS.13[BN] rats on high- and low-salt diets are given. Parameter values designated as "adjustable" are estimated from experimental data on individual rats from the 4 groups. The optimal values of these adjustable parameters are given in Table 5.

diet (Dyets, Bethlehem, PA) containing 0.4% NaCl with water provided ad libitum. Transmitters were implanted at 9 wk of age, and the animals were allowed to recover for 1 wk before pressures were collected for 3 days to ensure a steady state. The diet was then switched from 0.4% NaCl to 8% NaCl for 2 wk, and pressures again were collected for analysis. Pressure was collected at each salt level for 2 min at 100 Hz between 9 AM and 12 noon. All measurements were made in a sound attenuated room where rats were maintained in their home cage, placed on the receiver for the duration of the study. All protocols were approved by the Institutional Animal Care and Use Committee.

Signal processing. Because heart rate was not obtained in the above phenotyping protocol, experimental heart rate data used to parameterize the model was extracted from the arterial blood pressure time series data. This was done by first high-pass filtering the time series data and then detecting the time of zero-crossings of the pulse-pressure upstroke. The high-pass filter used was of the FIR class and from the Kaiser family of window functions. The fundamental frequency of the arterial pressure pulse corresponds to heart rate. By filtering frequency components lower than this fundamental frequency, both the arterial pressure offset as well as any slow oscillations are eliminated so that the pulse pressure is made to cross zero, allowing us to detect the time of zero-crossings of the pulse-pressure upstroke. We assume that the rat heart rate does not go <240 beats/min (4 Hz) under normal baseline physiological conditions. Therefore, the stop-band frequency of the Kaiser window was specified as 3 Hz and the pass band as 4 Hz. The stop-band attenuation and pass-band ripple were specified as 1×10^{-3} and 5.75×10^{-2}, respectively. The filter order and coefficients required to meet these specifications were calculated using MATLAB's Signal Processing Toolbox. The filter was applied to the data using MATLAB's filtfilt function. This function performs zero-phase digital filtering by processing the input data in both the forward and reverse directions; thus, the effects of filter phase distortion are minimized. Zero-crossings were detected using conditional statements in an iteration loop.

Noise in the arterial pressure recordings occasionally resulted in relatively large spikes appearing in the heart rate data. We assumed that, under normal physiological conditions, instantaneous changes in heart rate cannot exceed 50 beats/min, and we therefore removed data from any spikes exceeding this upper limit.

Parameter estimation. The overall model of baroreflex heart rate regulation is comprised of a system of eight ordinary differential equations. The differential equations are solved using MATLAB's solver ode23, an implementation of an explicit Runge Kutta 3(2) pair. The model contains a total of 13 adjustable parameters that are estimated for individual rats using the pressure heart rate data derived as described above. [In addition, three initial conditions $\varepsilon_2(0)$, $\varepsilon_3(0)$, and $c_{nor}(0)$ were estimated for each time series to compare model simulations to the data.] The parameters were estimated by fitting the model to the heart rate data using a genetic algorithm and least squares objective criterion given by

$$mse = \frac{1}{N_d} \sum_{i=1}^{N_d} \left(HR_{\text{model}}(t_i) - HR_{\text{data}}(t_i) \right)^2. \tag{22}$$

where *mse* is the mean square error, N_d is the number of data points, HR_{data} is experimental heart rate at time t_i, and HR_{model} is model predicted heart rate at time t_i. A single time course contained insufficient data to precisely identify all 13 model parameters, so we therefore used multiple datasets ($n = 6$ from the SS.13[BN] strain and $n = 9$ from the SS strain for both dietary conditions) from a number of individual rats from each of the four experimental groups studied to determine probability distributions and associated confidence bounds on parameter values to explain the data. Because initial conditions on

mechanics model parameters (see Fig. 3 and Table 1) for the highest expected arterial pressure estimated from the data. Where appropriate data was not available, upper and lower bounds were set to cover the broadest range of possible values that can be reasonably expected from initial optimization studies. All parameters were constrained to positive values. A list of initial parameter values, initial conditions, and upper and lower bounds, is given in Table 4. These initial values and bounds were used in the optimizations of each dataset from each experimental group of rats.

Because of the several nonlinear interactions between various components of our overall baroreflex model, typical gradient-based search methods could not be used. Such methods generally fail when applied to optimization problems involving nonsmooth nonconvex parameter landscapes. We instead relied on the stochastic search algorithms to fit our model to the experimental data. Unlike gradient-based methods, stochastic search algorithms such as simulated annealing and genetic algorithms are able to escape local minima and are ideally suited for these types of nonlinear global optimization problems. Genetic algorithms, in particular, are a powerful class of optimizers that can easily be parallelized. To fit the heart rate time course data, we have implemented a genetic algorithm based on PIKAIA (10) in the MATLAB environment. PIKAIA is an adaptive genetic algorithm employing decimal-encoding, crossover, elitism, fitness-based roulette-wheel selection, and an adaptive mutation rate. All optimizations in the present study were performed using our implementation of PIKAIA on a 128-node computational cluster.

RESULTS

Using aortic blood pressure as a model input, we fit model predicted heart rate to experimental heart rate with a genetic algorithm nonlinear optimization protocol and the least-squares objective criterion. The ability of our model to reproduce important features of the experimental heart rate time series data in the two strains of rat studied (results shown are from rats on low-salt diets) is illustrated by the examples shown in Fig. 8. Figure 8 demonstrates that the model is able to capture both the large relatively slow peaks (Fig. 8, *C* and *D*) as well as the relatively small but rapid oscillations (Fig. 8, *E* and *F*). We note, however, that the results shown in Fig. 8 represent cases where the model is able to reproduce these rapid oscillations particularly well and do not necessarily reflect model performance for all datasets. In some cases, the model was unable to reproduce these rapid transients, and the optimizer tended produce smooth fits through the data to minimize the sum of square error of the objective criterion. In most cases the model is able to fit the large slow peaks reasonably well. The fact that the model was able to capture both the slow and fast heart rate variations is striking given that most all parameters related to baroreflex dynamics (i.e., time constants) were fixed based on data from a different species.

The model was used to assess baroreflex function in four different experimental groups of rats including two genetic strains, the SS and SS.13[BN], on both low- and high-salt diets.
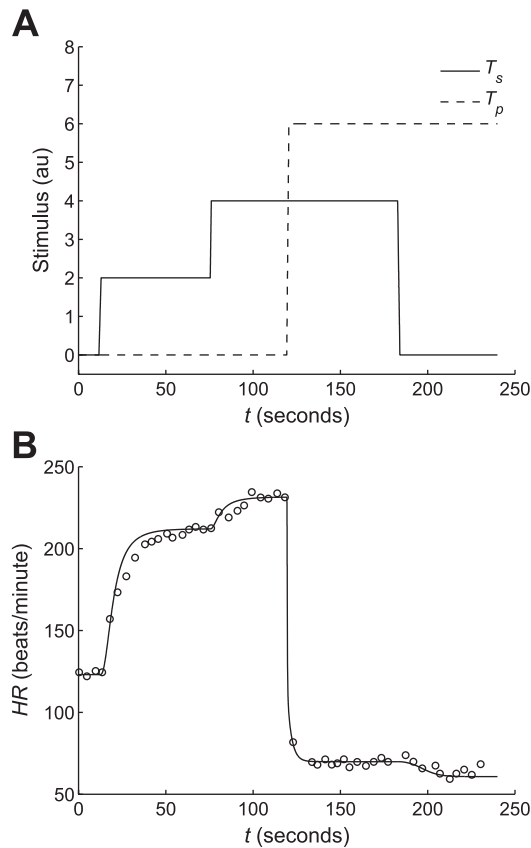
Fig. 7. Modeling the combined control of heart rate. The combined sympathetic and parasympathetic heart rate effector models is validated against heart rate response data collected from experiments of Warner and Russell (59) involving combined stimulation of cardiac sympathetic and vagal nerves. *A*: the sympathetic (T_s, dashed line) and parasympathetic (T_p, dotted line) stimuli applied in the Warner and Russell study served as inputs to the heart rate effector model. *B*: the heart rate effector model (solid line) is fit to the data (○) of Warner and Russell. The optimal parameter values used to produce the fit shown are HR_o = 123 beats/min, HR_{max} = 240 beats/min, HR_{min} = 60 beats/min, and β = 0.917. Values of all other parameters associated with model dynamics were not adjusted and were taken from model fits of Figs. 5 and 6.

variables with short time constants were arbitrarily selected, the objective criterion of *Eq. 22* was computed only for $t \geq 10$ s.

Parameter bounds were similarly set so that all possible parameter values fell within reasonably realistic physiological constraints as determined by available published data. For example, upper bounds of tone parameters were set so that the saturation effects of tone on heart rate (6, 18) could be reproduced without going to unrealistically high values. Similarly, upper and lower bounds on minimum, maximum, and intrinsic heart rate values were set using data from Bolter and Atkinson (6) and Nylander et al. (39). Upper bounds on strain initial conditions could be calculated using the pressure-radius relationship derived for rat aortas (see Fig. 2 and Table 1) and baroreceptor

Table 4. *Initial values and bounds for optimization*

	Parameter													Initial Condition		
	B_3	$\alpha_{s,o}$	$\alpha_{p,o}$	G_s	G_p	$T_{s,max}$	$T_{p,max}$	$T_{s,min}$	$T_{p,min}$	HR_o	HR_{max}	HR_{min}	β	$\varepsilon_{2,0}$	$\varepsilon_{3,0}$	$c_{nor,0}$
Initial value	225	59	66.2	0.2	0.2	4	3	0.5	0.5	280	586	230	0.1	0.232	0.149	1.249
Lower bound	25	0	0	0	0	0	0	0	0	250	450	50	0	0	0	0
Upper bound	300	96	144	0.5	0.5	8	5	2	2	450	650	250	1	0.378	0.297	5

Initial values, upper bounds, and lower bounds used in the optimization of adjustable parameters and initial conditions are given.
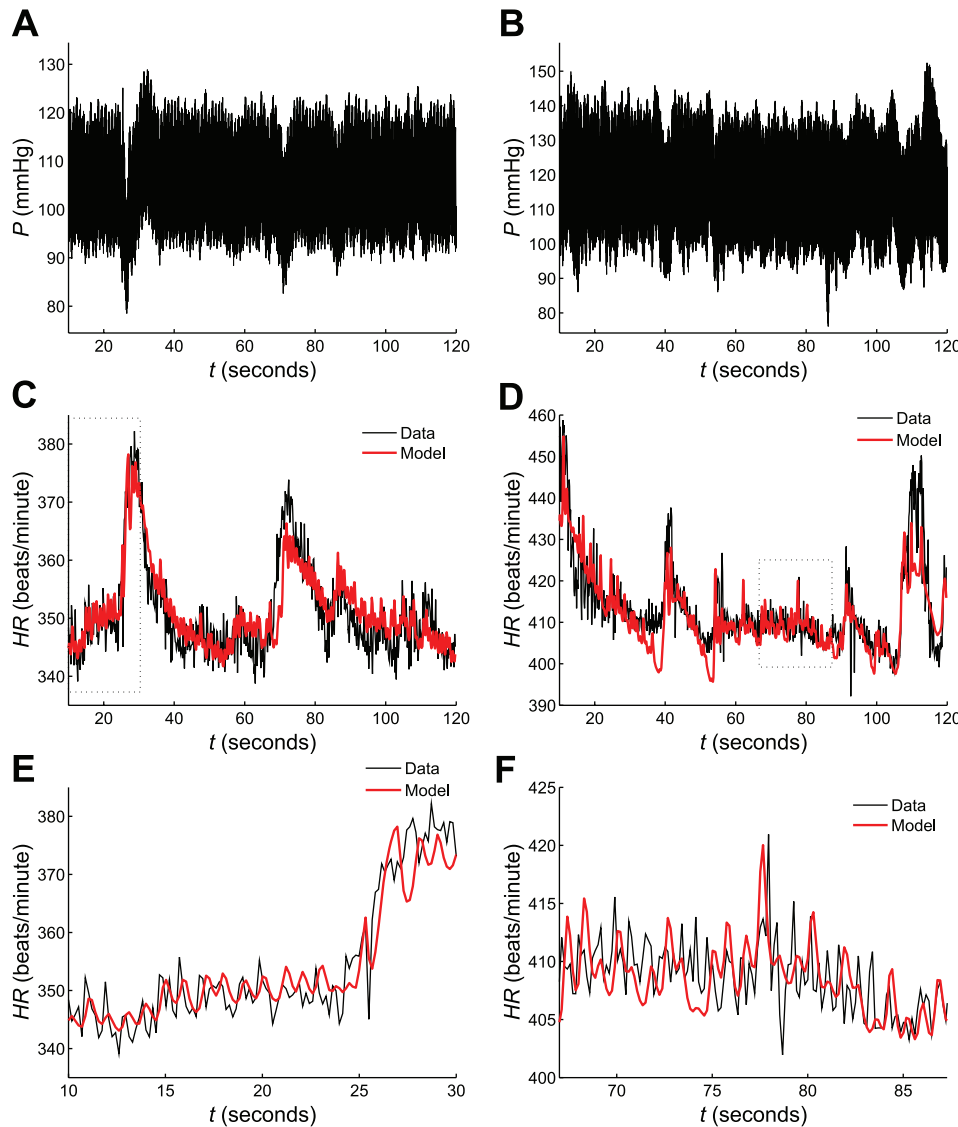
Fig. 8. Example fits of overall baroreflex model to heart rate data. The model of the overall baroreflex control of heart rate is able to simulate the major features of the heart rate data derived from Dahl SS and SS.13[BN] rat strains on low-salt diets. *A, B*: aortic blood pressure (*P*) 2-min time series data served as the input to the model. Data shown in *A* and *B* are from the SS and SS.13[BN] strains, respectively. Heart rate data of *C* and *D* were derived from the pulse pressure data of *A* and *B*, respectively. Optimal fits of our overall baroreflex model (red) to the heart rate data (black) demonstrate the ability of the model to capture many important features of the data including both the large slow peaks and the beat-wise oscillations. *E, F*: model fits of *C* and *D* are scaled to show 20-s segments where the model is able to reproduce beat-wise oscillations particularly well. Segments of data (black) and model fits (red) shown in *E* and *F* correspond to the boxes drawn in *C* and *D*, respectively.

The model was fit to a total of 12 datasets from the SS.13[BN] rats under each of the two experimental conditions (6 datasets for each condition), and a total of 18 datasets from SS rats under each of the two experimental conditions (9 datasets for each condition). The model-predicted heart rate time-series data (associated with the optimized parameter sets) is plotted along with experimentally derived heart rate data for each of the 12 datasets of the SS.13[BN] rats in Fig. 9 and for each of the 18 datasets of the SS rats in Fig. 10. As illustrated in Figs. 9 and 10, the model was able to capture most of the important features of each dataset. In some cases, the model tended to underestimate the magnitude of certain peaks or missed certain peaks entirely; however, in nearly every case the model was able to capture the general pattern of the data. A notable exception in which the model fails to capture the pattern of the data entirely is shown in Fig. 10*B, dataset 4*. The reasons for the poor fit of this dataset are not entirely clear.

Because the model explicitly accounts for the various subcomponents comprising the overall baroreflex, intermediate variables and parameters of interest can be estimated from the information contained in the data. The parameters estimated from the individual time courses are listed in Table 5. These include estimates of important quantities such as sympathetic and parasympathetic gains and offsets. The precision of parameter estimates is limited both by the amount of information contained in the heart rate data, which varies from dataset to dataset, as well as by the amount of interindividual variability of physiological parameters in each group (population) of rats. The averages and standard deviations of parameter estimates for each experimental group of rats, along with the optimal set of parameter values used to fit each individual dataset, are summarized in Table 5. Experimental mean arterial blood pressure and heart rate phenotype data for each group of rats is also given.

Figure 11 shows model-predicted (unmeasured) afferent baroreceptor firing rate, autonomic tone, and neurotransmitter concentrations associated with *dataset 2* of Fig. 9*A*. On the basis of model predictions for all individuals simulated, we may compare the levels of sympathetic and parasympathetic outflows in the baseline resting state between individuals and between experimental groups. Doing this, we assume that the telemetry recordings are taken from rats in a resting state. That
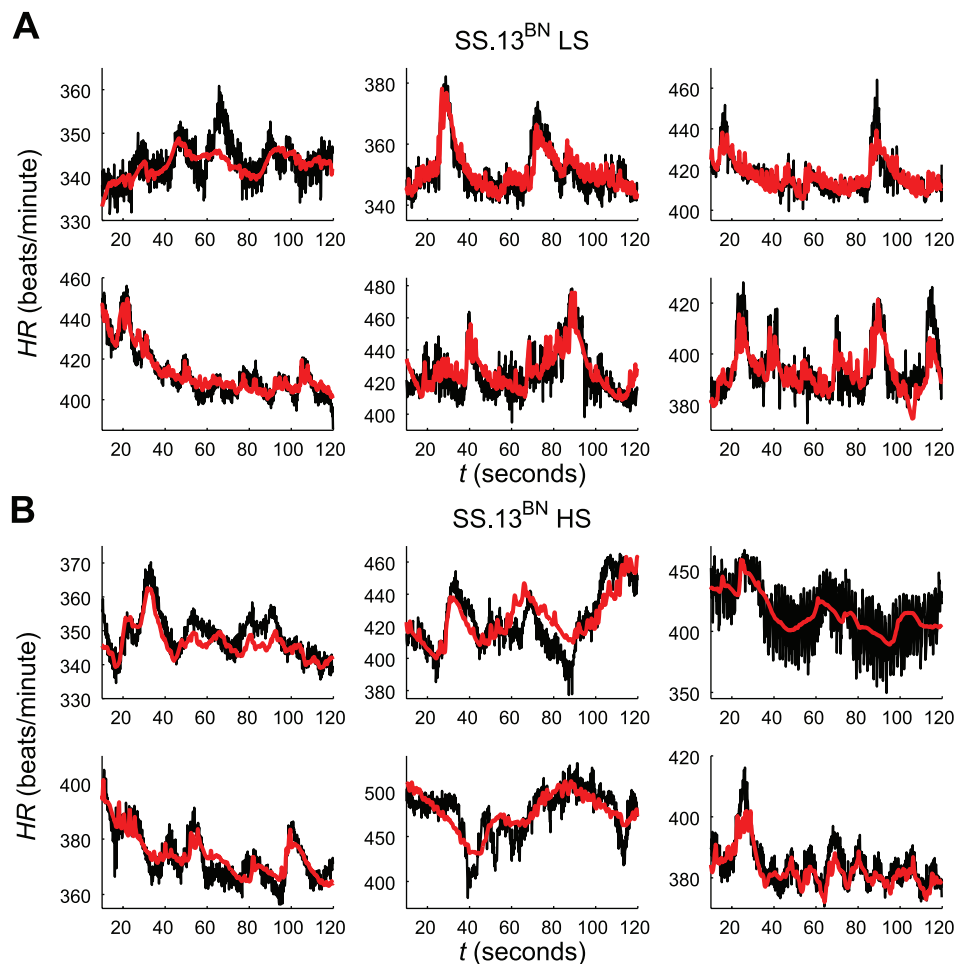
Fig. 9. Overall baroreflex model fits to heart rate data of SS.13^{BN} rats. Optimal model fits (red) to 6 datasets (black) each from SS.13^{BN} rats on low- *A* and high- *B* salt diets are shown. Each dataset of the 2 groups is from a different rat. The optimal parameter values associated with each dataset (numbered 1–6) of each group are given in Table 5.

is, it is assumed that no stressful stimuli are affecting the measurements. The predicted baseline autonomic outflows of each rat along with group means and standard deviations are summarized in Table 5.

To determine whether there are any statistically significant differences in mean parameter values between the SS and SS.13^{BN} rats on either high- or low-salt diet, we performed a one-way ANOVA on parameter estimates from each group of rats. To determine specifically which pairs of means differ statistically, we followed the ANOVA with the Dunn-Sidak multiple-comparisons test. This statistical analysis was also applied to group means of phenotype data (mean arterial blood pressure and heart rate) as well as model predictions (sympathetic and parasympathetic tones). Two outliers were removed prior to performing any statistics on the data. Here, an outlier was defined as a data point that is >1.5 times the interquartile range above the 75th or below the 25th percentile of the sample (the outliers are indicated in Table 5 with an asterisk). All parameter values associated with a given outlier dataset were excluded from statistical analysis, even if other parameters associated with the dataset were not outliers. One of the outliers was associated with *dataset 4* of the SS high-salt group; since the model was not able to fit this dataset, it was not surprising that its associated parameter values were outliers. The reason for the other outlier (*dataset 5* of the SS.13^{BN} high-salt group) excluded from the analysis was less clear. The

model appeared to produce a reasonable fit to the data; however, several important parameter estimates (most notably, the sympathetic and parasympathetic gains) of this dataset were quite different from estimates of other datasets of the same group.

Pairs of groups showing statistically significant differences are indicated symbolically in Table 5. Important results from the analysis are summarized in Fig. 12. In terms of experimental phenotype data, statistically significant differences in mean arterial pressure were detected between the SS rat on a high-salt diet and every other group as well as between the SS.13^{BN} high- and low-salt diet groups. No statistical differences were detected in mean heart rate between any of the four groups. Previously documented experimental findings in SR and SS rats suggest differences in the sympathetic and parasympathetic gain and offset parameters, G_s, G_p, $\alpha_{s,o}$, and $\alpha_{p,o}$, between these strains (2, 4, 20, 33, 61). Here, statistical differences in estimates of $\alpha_{s,o}$ were detected between the SS high-salt group and SS low-salt group, and between the SS high-salt group and the SS.13^{BN} low-salt group. There was also a trend toward a greater $\alpha_{s,o}$ in the SS.13^{BN} high-salt group compared with the two low-salt groups, but this was not found to be significant. The $\alpha_{p,o}$ parameter demonstrated a similar trend with an increase with high-salt diet in both strains. There also appeared to be a difference in $\alpha_{p,o}$ between the two strains with higher values in the SS strain; however, the only statisti-
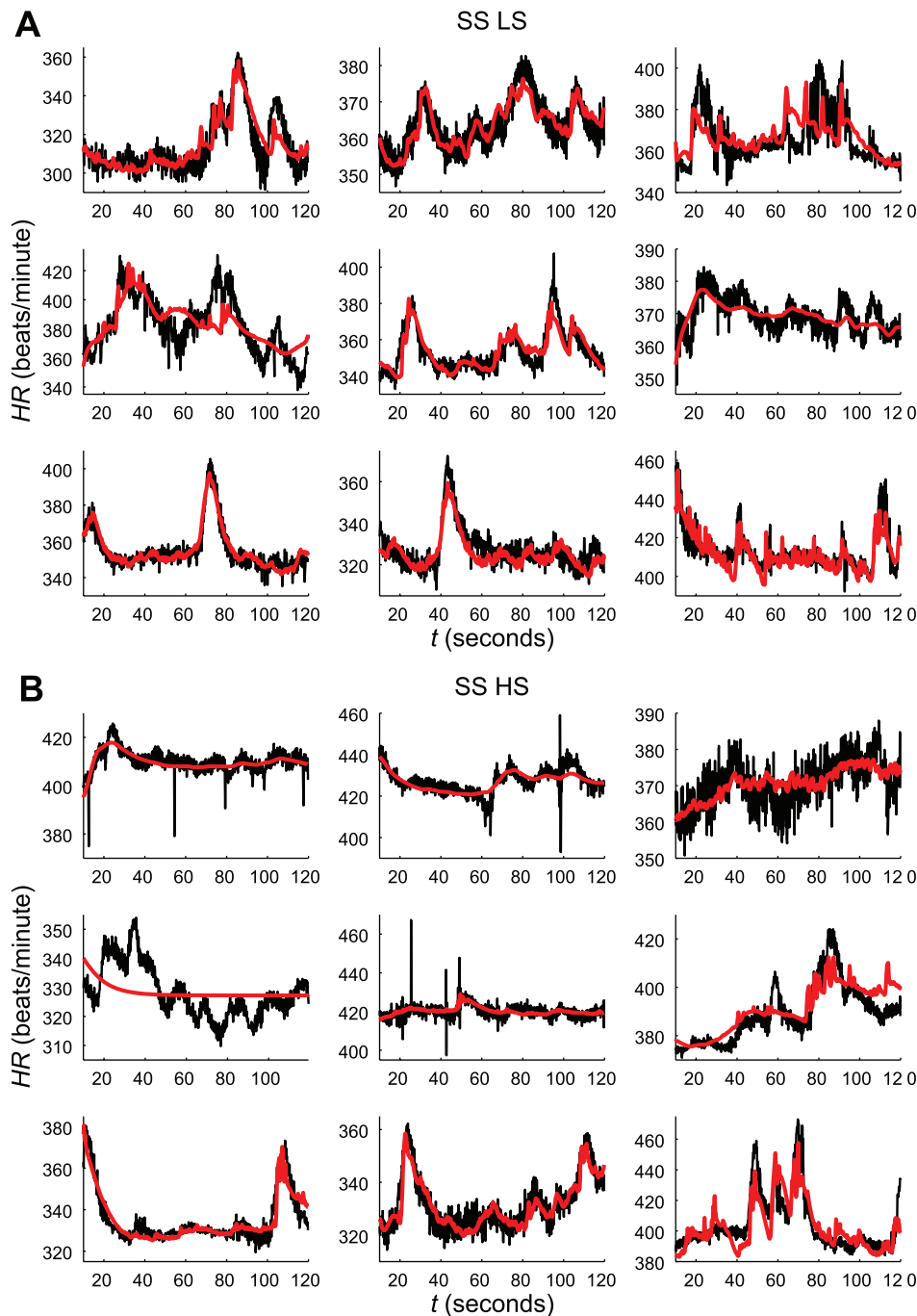
Fig. 10. Overall baroreflex model fits to heart rate data of SS rats. Optimal model fits (red) to 9 datasets (black) each from SS rats on low- (*A*) and high- (*B*) salt diets are shown. Each dataset of the 2 groups is from a different rat. The optimal parameter values associated with each dataset (numbered 1–9) of each group are given in Table 5.

cally significant difference detected in $\alpha_{p,o}$ was between the SS high-salt and SS.13[BN] low-salt groups. These model-based predictions that a high-salt diet elevates sympathetic and parasympathetic offset in the SS rat and that there exists a defect in parasympathetic offset in SS compared with SS.13[BN] rats require further experimental investigation.

The gain parameters also revealed interesting physiological differences between the different groups of rats. Our results show a mild attenuation in G_s in SS.13[BN] rats on a high-salt diet and a much larger attenuation of G_s in SS rats on a high-salt diet. The SS rats on a low-salt diet were found to have the highest sympathetic gain (G_s) among all four groups, and statistically significant differences between the SS low-salt

group and the two high-salt groups were detected. It is interesting that SS, and not the SS.13[BN] rat, which is known to be protected from developing hypertension, has the highest gain on a low-salt diet. No statistical differences were detected in the parasympathetic gain (G_p) between any of the four groups. This suggests that the central/peripheral nervous systems may play some role in the baroreflex dysfunction observed in the SS rat on a high-salt diet. Specific conclusions drawn from these data are that a high-salt diet selectively attenuates the sympathetic gain and that SS.13[BN] rats are protected from this attenuation. There may be an intrinsic difference in sympathetic gain that is associated with a lower gain in the SS.13[BN] rats, but this finding is not significant. One parameter we were

Table 5. *Results*

Dataset	Phenotype Data		Parameter Values													Initial Conditions			Model Predictions		Goodness-of-fit
	MAP	HR	$\alpha_{s,o}$	$\alpha_{p,o}$	B_3	$T_{s,max}$	$T_{p,max}$	$T_{s,min}$	$T_{p,min}$	G_s	G_p	HR_o	HR_{max}	HR_{min}	β	$\varepsilon_{2,0}$	$\varepsilon_{3,0}$	$c_{nor,0}$	T_s	T_p	sse
SS.13BN LS																					
1	109.003	342.944	58.565	76.019	206.973	4.120	4.994	0.488	1.594	0.178	0.492	282.648	483.218	226.238	0.175	0.183	0.161	1.441	1.073	1.726	14.757
2	103.857	351.401	51.287	67.352	207.383	4.487	4.906	0.314	1.055	0.140	0.264	310.114	643.874	230.146	0.019	0.148	0.134	0.809	0.777	3.025	21.327
3	112.349	416.992	59.073	59.128	129.992	4.235	2.184	0.303	0.469	0.133	0.229	346.166	589.374	228.150	0.035	0.250	0.154	1.428	1.157	0.604	30.349
4	114.185	414.840	57.438	66.043	169.760	2.641	2.184	1.038	0.597	0.210	0.299	275.814	570.148	240.260	0.003	0.190	0.185	2.183	1.232	1.650	24.712
5	106.236	426.046	57.454	69.359	80.993	5.292	4.646	0.707	0.444	0.180	0.356	266.242	605.180	229.184	0.019	0.291	0.116	1.520	1.297	2.796	85.651
6	111.148	394.530	59.226	67.585	25.041	3.784	1.675	0.530	0.462	0.204	0.433	268.598	589.120	236.024	0.184	0.197	0.157	0.782	0.808	1.421	58.425
Average	109.463‡˘	391.125˘	57.174*˘	67.581˘	136.690	4.093	3.172	0.563	0.770	0.174	0.346	291.597	580.152	231.667	0.073	0.210	0.151	1.360	1.057	1.870	39.203
Std dev	3.887	35.671	2.985	5.445	72.998	0.874	1.907	0.277	0.465	0.032	0.102	31.054	53.570	5.351	0.084	0.052	0.024	0.520	0.219	0.901	27.322
SS.13BN HS																					
1	143.025	349.966	62.630	93.491	299.857	7.980	4.915	0.452	1.583	0.134	0.495	252.406	605.018	223.886	0.009	0.200	0.200	0.822	0.700	2.133	17.821
2	135.270	420.915	76.637	91.992	164.043	7.998	0.219	0.422	0.022	0.170	0.380	361.720	649.730	194.460	0.142	0.241	0.055	0.056	0.585	0.204	133.379
3	130.709	417.266	60.463	69.566	133.169	5.513	4.689	0.493	0.342	0.124	0.185	251.912	589.130	220.472	0.068	0.278	0.228	1.538	1.204	3.573	332.913
4	132.179	373.785	60.381	79.855	249.345	4.705	4.345	0.704	1.291	0.105	0.493	288.672	597.654	232.724	0.020	0.198	0.175	1.377	1.031	3.805	23.672
*5	137.441	478.752	71.893	110.222	224.812	7.983	3.543	1.146	0.365	0.412	0.075	270.350	549.692	247.692	0.310	0.374	0.213	4.860	2.352	0.714	280.178
6	142.861	384.565	63.109	81.940	286.173	6.394	2.541	0.668	0.441	0.132	0.128	254.848	649.110	227.188	0.661	0.229	0.201	1.124	0.849	1.960	22.250
Average	136.914	404.208	65.852	87.844	226.233	6.762	3.375	0.648	0.674	0.180	0.293	279.985	606.722	224.404	0.201	0.253	0.179	1.630	1.120	2.065	135.036
Std dev	5.227	45.299	6.778	14.019	66.450	1.444	1.773	0.270	0.615	0.116	0.187	42.496	38.193	17.502	0.251	0.066	0.063	1.667	0.643	1.457	140.774
*Average	136.809†˘	389.299˘	64.644	83.369	226.517	6.518	3.342	0.548	0.736	0.133˘	0.336	281.912	618.128	219.746*	0.180	0.229	0.172	0.983	0.874	2.335	106.007
*Std dev	5.837	29.966	6.817	9.768	74.289	1.470	1.981	0.129	0.667	0.024	0.171	47.218	29.114	14.840	0.274	0.033	0.068	0.585	0.249	1.451	135.837
SS LS																					
1	120.096	313.935	60.047	80.473	125.356	6.998	3.584	0.664	0.532	0.499	0.282	271.776	547.758	230.244	0.049	0.250	0.120	0.096	0.719	2.625	64.363
2	133.117	362.817	69.579	79.826	31.006	3.937	1.831	0.605	0.684	0.179	0.167	262.752	582.230	231.372	0.317	0.157	0.157	1.259	0.769	1.577	16.469
3	111.713	366.699	56.325	72.737	293.727	6.482	4.757	0.977	0.610	0.499	0.408	286.002	581.990	244.654	0.459	0.237	0.131	0.082	0.992	3.552	104.102
4	111.942	380.206	57.096	70.407	295.394	3.543	4.926	0.728	0.032	0.194	0.498	251.644	577.296	235.544	0.104	0.144	0.142	0.017	0.896	3.672	200.593
5	119.351	353.195	56.686	76.648	123.247	5.758	4.559	0.591	0.262	0.293	0.324	259.778	610.446	237.706	0.090	0.206	0.152	0.753	0.610	3.261	38.549
6	121.651	368.554	58.574	110.838	33.168	4.368	4.570	1.040	0.492	0.106	0.000	280.422	592.470	243.640	0.809	0.190	0.188	0.524	1.379	2.531	18.017
7	115.965	355.321	58.020	79.173	117.089	3.138	4.760	0.440	1.367	0.158	0.497	263.394	599.404	235.980	0.070	0.157	0.156	0.776	0.654	2.382	17.229
8	109.250	329.432	51.583	72.393	255.054	7.998	4.540	0.422	0.034	0.500	0.499	255.966	649.932	248.364	0.008	0.146	0.143	0.605	0.423	2.067	32.833
9	116.560	414.871	61.194	68.561	52.544	5.344	2.696	0.839	0.016	0.489	0.219	282.746	588.394	246.394	0.070	0.163	0.162	1.523	0.931	2.111	42.262
Average	117.738˘	360.559˘	58.790˘	79.006	147.398	5.285	4.025	0.701	0.448	0.324‡˘	0.322	268.276	592.213	239.322‡	0.220	0.183	0.150	0.626	0.819	2.642	59.380
Std dev	7.128	28.868	4.870	12.687	107.521	1.668	1.090	0.218	0.433	0.171	0.173	12.440	27.688	6.638	0.265	0.040	0.020	0.525	0.274	0.716	59.924
SS HS																					
1	195.482	409.319	74.901	74.929	200.805	4.857	4.066	1.517	1.699	0.063	0.422	279.254	583.278	234.240	0.185	0.267	0.265	1.285	1.677	4.066	12.164
2	196.932	428.117	71.593	73.267	278.404	8.000	4.701	1.281	0.892	0.059	0.234	270.028	587.306	245.578	0.009	0.200	0.162	1.862	1.401	4.701	18.871
3	166.097	370.223	57.015	116.785	296.915	2.951	2.495	0.749	1.021	0.042	0.496	272.800	581.720	244.858	0.047	0.219	0.170	0.880	0.921	1.678	30.668
*4	156.449	327.808	34.380	40.382	251.641	7.719	2.392	0.917	1.997	0.392	0.357	250.210	526.408	233.250	0.657	0.283	0.239	1.056	0.923	2.392	76.526
5	186.995	420.262	76.239	103.771	186.733	7.994	4.936	1.745	1.522	0.139	0.450	278.076	597.134	228.432	0.041	0.287	0.269	1.705	1.779	4.844	14.069
6	181.641	388.409	59.162	110.807	26.504	3.896	4.427	0.242	0.997	0.017	0.494	261.420	595.960	227.460	0.097	0.179	0.142	1.422	1.187	3.943	46.852
7	168.416	335.630	83.147	104.370	25.011	5.760	4.985	1.004	0.860	0.199	0.500	290.264	560.946	230.316	0.384	0.105	0.100	3.071	1.036	4.642	23.908
8	145.508	330.925	62.951	77.705	25.074	5.662	1.141	0.554	0.110	0.131	0.061	318.070	579.994	224.752	0.032	0.257	0.182	0.796	0.633	0.892	24.251
9	146.125	404.124	67.378	87.127	194.458	7.148	3.603	0.592	0.113	0.190	0.272	263.896	647.544	241.492	0.445	0.265	0.214	0.701	0.759	2.451	117.850
Average	171.516	379.424	65.196	87.683	165.061	5.999	3.638	0.956	1.024	0.137	0.365	276.002	584.477	234.486	0.211	0.229	0.194	1.420	1.146	3.290	40.573
Std dev	19.842	39.753	14.327	24.049	111.101	1.852	1.348	0.487	0.648	0.115	0.150	19.552	32.079	7.741	0.231	0.060	0.057	0.737	0.399	1.463	35.225
*Average	173.400†‡˘	385.876	69.048†˘	93.595†˘	154.238	5.783	3.794	0.960	0.902	0.105˘	0.366	279.226	591.735	234.641‡	0.155	0.222	0.188	1.465	1.174	3.402	36.079
*Std dev	20.333	37.119	9.053	17.360	113.587	1.856	1.351	0.520	0.573	0.069	0.161	18.166	25.182	8.261	0.170	0.060	0.059	0.775	0.417	1.522	34.790

Optimal estimates of the adjustable parameters used to produce the model fits shown in Figs. 9 and 10 are listed. Also given are mean arterial pressure (*MAP*) and mean heart rate (*HR*) phenotype data associated with each dataset along with predicted baseline sympathetic (T_s) and parasympathetic (T_p) tones, optimal values of adjustable initial conditions, and the sum of square errors (*sse*) associated with each model fit. *Outlier datasets (described in text). Averages and SD (denoted as "std dev" in the table) of all group data as well as averages and SD of group data with outliers excluded (*) are shown. Statistical differences ($P < 0.05$) between groups are denoted by †, ‡, ˘, and ˘. Outliers were excluded from all statistical analyses. Key: † vs. SS.13BN LS; ‡ vs. SS.13BN HS; ˘ vs. SS LS; ˘ vs. SS HS.
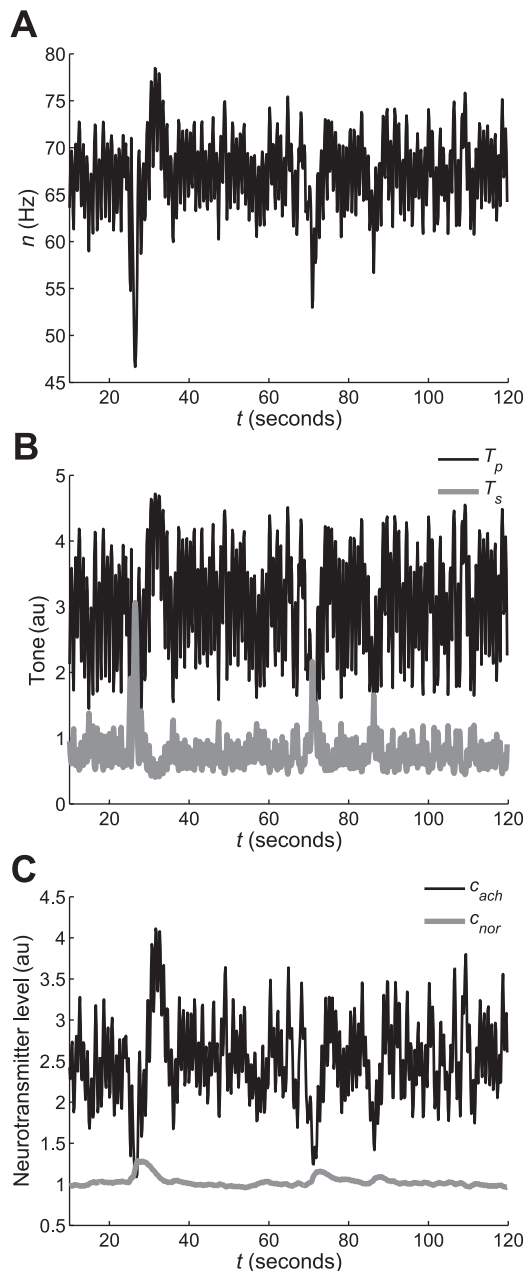
Fig. 11. Overall baroreflex model predictions. Unmeasured physiological properties associated with the various components of the baroreflex system are predicted from heart rate data using the model. The model predictions shown are associated with the optimal fit of our model to *dataset 2* of the SS.13[BN] low-salt group. *A*: predicted afferent baroreflex firing rate (n); *B*: sympathetic (T_s) and parasympathetic (T_p) tones; *C*: norepinephrine (c_{nor}) and acetylcholine (c_{ach}) concentrations are shown.

highest in the SS rat on a high-salt diet. Furthermore, a high-salt diet was shown to elevate T_s in the SS strain and to reduce T_s in the SS.13[BN] strain. On the other hand, as shown in Fig. 12*H*, parasympathetic tone (T_p) was higher in the SS strain on both high- and low-salt diet, and a high-salt diet elevated T_p in both strains. These results are in line with the finding of a selective sympathetic defect in the SS rat. It would seem that the SS.13[BN] rat is able to compensate any potential increases in blood pressure that would otherwise be induced by a high-salt diet through sympathetic withdrawal. The SS rat, on the other hand, is unable to exert this sympathetic withdrawal compensation, possibly because of the observed defects in sympathetic gain with high-salt diet, which therefore manifests as an increased sympathetic tone with a high-salt diet. This increase in sympathetic tone may then contribute to the increased blood-pressure phenotype observed in this strain with a high-salt diet. On the other hand, because parasympathetic gains are identical between the two strains and unaffected by diet, the parasympathetic outflows are effectively increased with high-salt diet in both strains as would be expected.

DISCUSSION

Using a mechanistic modeling approach, we are able to explain a number of previously published experimental findings related to baroreflex dysfunction in the Dahl SS rat. Furthermore, we have uncovered a number of important differences in baroreflex physiology between the SS and consomic SS.13[BN] rats on high- and low-salt diets and have for the first time associated chromosome 13 of the Dahl rat with dysfunction of the baroreflex control system. Studies have demonstrated a sympathetic defect in SS rats on high-salt diets (33) but not on low-salt diets (20). This defect with high-salt diet can be explained by the attenuated sympathetic gain and therefore blunted sympathetic withdrawal in the SS rat on high-salt diet as demonstrated in this study. Furthermore, previous studies have demonstrated an increased afferent baroreceptor pressure threshold in both the SS and SR rat on a high-salt diet (2). It is difficult to make any conclusions related directly to the afferent baroreceptor component in this study because parameters of that component were fixed in our analysis. However, the sympathetic and parasympathetic offset parameters were adjustable and were informed by experimental data, and these parameters reflect composite differences in thresholds of both the afferent and central components of the reflex. We found increased sympathetic offset with high-salt diet in the SS rat which may be related to an increased afferent baroreceptor pressure threshold as described previously.

An important difference in SS and SS.13[BN] physiology uncovered through our analysis includes a markedly reduced attenuation of sympathetic gain with high-salt diet in the SS.13[BN] rat. In addition, model predictions of sympathetic and parasympathetic outflows revealed an interesting trend that we used to develop a new hypothesis related to baroreflex dysfunction in the SS rat. Model analysis predicts that high-salt diet reduces sympathetic tone in the SS.13[BN] rats, whereas it causes elevation of sympathetic tone in the SS rat. If real, this apparent defect in sympathetic withdrawal in the SS rat on high-salt diet may be due to a defect in sympathetic gain. Thus, a defect in sympathetic gain, leading to increased sympathetic outflow, may be playing a role in the blood pressure phenotype

surprised to detect a significant difference in was the minimum heart rate, which was found to be significantly lower in the SS.13[BN] high-salt group compared with both SS groups. It is unclear why this parameter is lower in this particular group and what the implications of this difference may be. Again, these model-based predictions require experimental verification.

While model predictions failed to reveal any statistically significant differences in sympathetic or parasympathetic outflows between any of the four groups, an interesting trend emerges. Figure 12*G* reveals that sympathetic tone (T_s) is
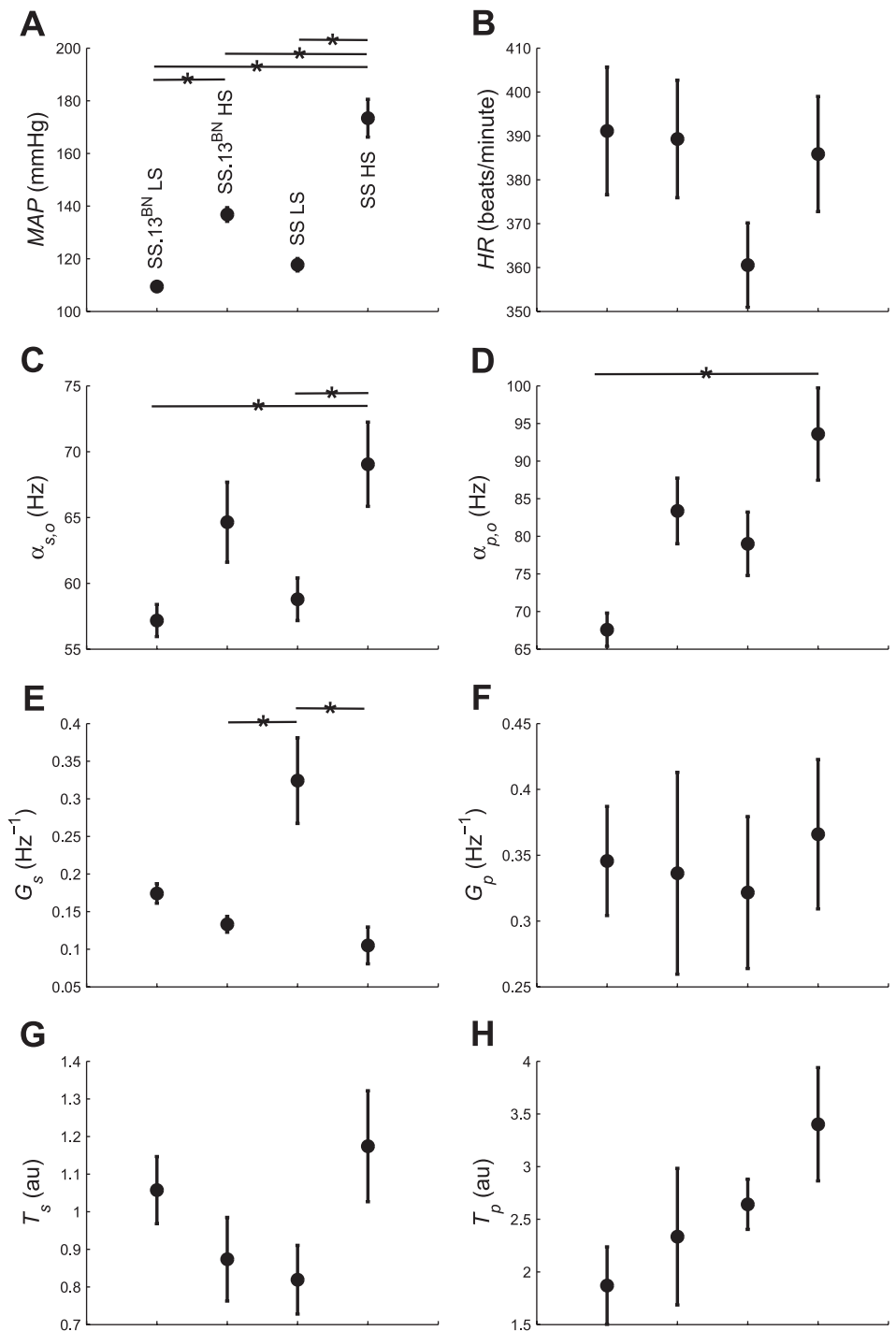
Fig. 12. Graphical summary. Selected phenotype, parameter value, and model prediction data are summarized for each experimental group. Ordering of groups in all panels is the same as in *A*. ● Group means; error bars represent standard errors of the means; *significant ($P < 0.05$) differences between pairs of means. Mean arterial blood pressure (*MAP*) and mean heart rate (*HR*) phenotype data are shown in *A* and *B*, respectively. Sympathetic offset ($\alpha_{s,o}$), parasympathetic offset ($\alpha_{p,o}$), sympathetic gain (G_s), and parasympathetic gain (G_p) parameter value data are shown in *C*, *D*, *E*, and *F*, respectively. Model predictions of mean baseline sympathetic (T_s) and parasympathetic (T_p) tone data are shown in *G* and *H*, respectively.

of the SS rat on a high-salt diet. This hypothesis requires further testing by collecting a larger sample size to increase the power of our analysis and also by collecting direct measurements of autonomic outflows and validating our model against these measurements.

This hypothesis implicates at least some neural contribution of chromosome 13 to the salt-sensitive hypertension phenotype of the Dahl SS rat. Though originally hypothesized to be primarily a defect in renal and humoral factors, neural mechanisms were later explored and shown to play an important role in the pathogenesis of the disease (31, 37). We believe that

Dahl SS hypertension cannot be explained by a single mechanism or defect, and that renal, humoral, endocrine, neural, and hemodynamic factors are all involved in some way (31, 37, 43). However, the relative contributions of each of these factors and their genetic associations are not well known. A major advantage of the modeling approach in general is the ability to integrate the effects of multiple physiological controllers on whole system behavior so that the relative roles of the various controllers in salt-sensitive hypertension may be better elucidated. The baroreflex model developed here represents an important starting point in this effort.

Though we were able to confirm a number of previous findings, our results conflict with some previously published findings. For example, Whitescarver et al. (61) concluded that baroreflex dysfunction in SS rats is due to a parasympathetic defect. However, our results failed to identify any differences in parasympathetic physiology between any of the strains studied. In addition, studies have shown a defect in afferent baroreceptor sensitivities in SS rats, even on low-salt diet (4, 33). We were unable to definitively identify any dysfunction in baroreflex gain in the SS rat on low-salt diet. There are many possible explanations for these discrepancies. For example, all of these previous studies used the SR rat as a control, which has very different genetics and possibly very different physiology than the consomic SS.13^{BN} control rat used in the present study. Thus, differences between SS and SR rat may not exist between the SS and SS.13^{BN} rat. (Note that the SS.13^{BN} retains some of the salt-sensitivity of the SS strain.) In addition, the measurements performed in these studies often relied on pharmacological manipulations or invasive surgical procedures involving anesthesia. Such perturbations may themselves be expected to alter the function of the physiological control systems of interest or, at the very least, may alter the physiological state of the animal. Thus, the findings may depend on the experimental conditions and may not necessarily hold in the animals' baseline resting state. Our experimental approach relied on a telemetry protocol to minimize the effects of stressors on our measurements. In addition, the parameters of our model are, theoretically, less dependent on operating points since they explicitly account for many of the nonlinearities of the control systems of interest. In this case, the model parameters would be expected to hold under a wider variety of experimental conditions.

Despite that fact, it is crucial to note that the precision of our parameter estimates is highly dependent on the sensitivity of our model to those parameters. This sensitivity is dependent on both the data used to estimate the parameters as well as the structure of the model itself. Concerning the structure of the model, we have accounted for a number of known nonlinear features of the baroreflex system that tend to increase the complexity of the parameter landscape. Nonlinearities such as saturation can lead to a number of local minima in the solution space. We have addressed these difficulties by using optimizers ideally suited to overcome these local minima, but the likely possibility exists that our parameter estimates do not correspond to the global minima. With regard to the data, it may be difficult to obtain sensitive estimates of all parameters using heart rate data alone. Heart rate datasets containing a number of large peaks and valleys are rich in information pertaining to the baroreflexes and would be expected to confer a higher sensitivity of the model to the parameters, whereas a dataset containing a relatively constant heart rate contains less information about the baroreflexes and could potentially be explained by several alternative combinations of parameter values (and therefore, would confer less sensitivity of the estimates to the data). Most previous modeling studies of the overall baroreflex addressed this problem by perturbing the system in some way such as a sit-stand maneuver (40) or the Valsalva maneuver (30). Pharmacological interventions such as phenylephrine and sodium nitroprusside have also been used as a means of perturbing the system (20, 33); such interventions allow the response of the baroreflex system to be assessed

under extreme physiological conditions and offer a means of challenging the model at these extremes. In the present study, we identify parameters using only the naturally occurring spontaneous fluctuations in heart rate. The current model can be used to design experiments using dynamic perturbations to improve the precision of parameter estimates.

In addition to the physiological insights into Dahl salt-sensitive hypertension gained through our modeling analysis as described above, the model developed here can serve as a powerful tool for analyzing and integrating data from different components of the baroreflex and may be valuable in helping us better understand the general function of and interaction between various components of the overall reflex. As far as we are aware, this work represents the most mechanistically detailed available model of the overall baroreflex heart rate control system in the rat. Ideally, parameters of our model would be identified with detailed measurements of each of the components of the baroreflex for each of our experimental rat strains. Although these data are not available for the rat strains used in the present study, such detailed measurements exist from other strains and from other species. With the assumption that there are no differences between strains or species in certain model parameters, we are able to take advantage of these available data. Specifically, we have demonstrated that baroreceptor dynamics parameters from the WKY rat and heart rate dynamics parameters from mongrel dogs allow us to effectively simulate heart rate data from SS and SS.13^{BN} rats. We expect that many of the parameter values used in the present model are conserved across species; it would therefore be interesting to see whether the model is able to explain differences in the baroreflex control system in different animal models of baroreflex dysfunction or in human studies.

A remarkable feature of these fits is their ability to capture both the slow and fast variations in heart rate as illustrated in Fig. 8. These two types of variation are believed to be mediated separately by the sympathetic and parasympathetic nervous systems and thought to be a consequence of the different time constants associated with the two nervous systems. It is believed that the shorter time constants of the parasympathetic pathway allow it to exert beat-by-beat control, while the longer time constants associated with the sympathetic pathway are associated with relatively smoother and slower variations in heart rate (28, 34, 35). By accounting for these differences in time constants, we are able to simulate these disparate effects of the two pathways on heart rate.

However, the model is unable to capture the fast dynamics of the parasympathetic nervous system in all of the datasets. We can speculate a variety of explanations for this, the simplest being that there is some variation in either baroreceptor or PNS/sinus node dynamics among different individuals and that additional parameters must be made adjustable to capture these dynamics. The other explanation is that the smoother fits through the data represent local minima in the solution space. This would also explain why the parameters estimates of the parasympathetic nervous system were less precise than those of the sympathetic nervous system and may be a reason why we were unable to detect differences in parameters of the parasympathetic nervous system between the different rat strains studied. Furthermore, our model neglects the delays associated with both the sympathetic and parasympathetic nervous systems because they were assumed to be negligibly small in the

rat (28, 41). However, even small delays in the parasympathetic nervous system could greatly affect the phase of the fast heart rate variations. If these variations were out of phase, the smooth fits observed with many datasets could represent actual global minima. Finally, even in those datasets for which the model is able to capture the fast variations, the model was never able to perfectly capture all of the data. It is not clear whether peaks not captured by the model represent important physiological processes, physiological noise, or noise associated with the processing of the heart rate data from the blood pressure data. It will be interesting to see whether better fits of these fast dynamics can be achieved by accounting for system delays to correct for phase differences, by analyzing heart rate in the frequency domain, or by attaining actual ECG heart rate measurements to eliminate any noise introduced through our signal processing protocol.

The performance of the model in capturing the smoother slower peaks associated with the sympathetic nervous system was generally better. This may be reflected in the higher precision of the sympathetic gain estimates compared with the parasympathetic estimates. However, although the model was able to capture the general pattern of most of these peaks, the magnitude of the peaks was often underestimated. In addition, not all of the peaks could be simulated by the model. This suggests that the model may be missing some important dynamic of the baroreflex control of heart rate, or that some other physiological control mechanism(s) is at play. We have, for example, made several simplifications in the baroreflex control system such as neglecting contributions from unmyelinated fibers. Brown et al. (9) demonstrated differences in frequency responses between myelinated and unmyelinated fibers. In addition, Seagard et al. (50) identified two types of baroreceptor responses (type I and type II), but the model accounts for only type I response. Another simplification of our model was the assumption that the CNS acts as an all-pass filter. Many studies have demonstrated that this is not the case and suggest that filter behavior at the CNS may play an important role in baroreflex dynamics (23, 24, 41, 46, 47). The model also ignores contributions from the baroreceptors in the carotid sinus. Pressures in the carotid sinus can be quite different from those in the aortic arch, and accounting for the relative contributions of the baroreceptors of the carotid sinus may be required to achieve better fits. Finally, many other physiological controllers are known to be involved in the autonomic reflexes including the chemoreceptors, cardiopulmonary receptors, and others. It is therefore unrealistic to expect to simulate all features of the heart rate data using a model of only the baroreflex system. The model developed in this study may easily be adapted to include contributions from other fiber types and from carotid sinus baroreceptors. In addition, the model serves as a module that may be incorporated into a more comprehensive cardiovascular model. In this manner, the relative roles of different physiological systems in the control of heart rate may be dissected more completely, and we may begin to elucidate the relative roles and interactions between the various components of arterial blood pressure regulation so that a deeper understanding of the physiological origins of blood pressure salt-sensitivity becomes within closer reach.

DISCLOSURES

No conflicts of interest, financial or otherwise, are declared by the authors.

REFERENCES

1. **Alfrey KD.** *A Model of the Aortic Baroreceptor in Rat* (MS thesis). Houston, TX: Rice University, 1997.
2. **Andresen MC.** High-salt diet elevates baroreceptor pressure thresholds in normal and Dahl rats. *Circ Res* 64: 695–702, 1989.
3. **Andresen MC.** Short- and long-term determinants of baroreceptor function in aged normotensive and spontaneously hypertensive rats. *Circ Res* 54: 750–759, 1984.
4. **Andresen MC, Rudis SK, Bee DE.** Aberrant baroreceptor mechanotransduction in adult Dahl rats on low-salt diet. *Am J Physiol Heart Circ Physiol* 256: H446–H454, 1989.
5. **Beard DA, Kushmerick MJ.** Strong inference for systems biology. *PLoS Comput Biol* 5: e1000459, 2009.
6. **Bolter CP, Atkinson KJ.** Maximum heart rate responses to exercise and isoproterenol in the trained rat. *Am J Physiol Regul Integr Comp Physiol* 254: R834–R839, 1988.
7. **Bristow JD, Honour AJ, Pickering GW, Sleight P, Smyth HS.** Diminished baroreflex sensitivity in high blood pressure. *Circulation* 39: 48–54, 1969.
8. **Brown AM, Saum WR, Tuley FH.** A comparison of aortic baroreceptor discharge in normotensive and spontaneously hypertensive rats. *Circ Res* 39: 488–496, 1976.
9. **Brown AM, Saum WR, Yasui S.** Baroreceptor dynamics and their relationship to afferent fiber type and hypertension. *Circ Res* 42: 694–702, 1978.
10. **Charbonneau P, Knapp B.** *A User's Guide to PIKAIA 1.0, NCAR Technical Note 418+IA.* Boulder, CO: National Center for Atmospheric Research, 1995.
11. **Cowley AW Jr.** Long-term control of arterial blood pressure. *Physiol Rev* 72: 231–300, 1992.
12. **Cowley AW Jr, Roman RJ, Kaldunski ML, Dumas P, Dickhout JG, Greene AS, Jacob HJ.** Brown Norway chromosome 13 confers protection from high salt to consomic Dahl S rat. *Hypertension* 37: 456–461, 2001.
13. **Di Rienzo M, Parati G, Radaelli A, Castiglioni P.** Baroreflex contribution to blood pressure and heart rate oscillations: time scales, time-variant characteristics and nonlinearities. *Philos Transact A Math Phys Eng Sci* 367: 1301–1318, 2009.
14. **Eckberg DL.** Arterial baroreflexes and cardiovascular modeling. *Cardiovasc Eng* 8: 5–13, 2008.
15. **Eckberg DL.** Nonlinearities of the human carotid baroreceptor-cardiac reflex. *Circ Res* 47: 208–216, 1980.
16. **Franz GN.** Nonlinear rate sensitivity of the carotid sinus reflex as a consequence of static and dynamic nonlinearities in baroreceptor behavior. *Ann NY Acad Sci* 156: 811–824, 1969.
17. **Glick G, Braunwald E.** Relative roles of the sympathetic and parasympathetic nervous systems in the reflex control of heart rate. *Circ Res* 16: 363–375, 1965.
18. **Goldberger JJ, Challapalli S, Tung R, Parker MA, Kadish AH.** Relationship of heart rate variability to parasympathetic effect. *Circulation* 103: 1977–1983, 2001.
19. **Gonzalez ER, Krieger AJ, Sapru HN.** Central resetting of baroreflex in the spontaneously hypertensive rat. *Hypertension* 5: 346–352, 1983.
20. **Gordon FJ, Mark AL.** Mechanism of impaired baroreflex control in prehypertensive Dahl salt-sensitive rats. *Circ Res* 54: 378–387, 1984.
21. **Hauss WH, Kreuziger H, Asteroth H.** über die reizung der pressorezeptoren im sinus caroticus beim hund. *Z Kreislaufforsch* 38: 28–33, 1949.
22. **Katona PG, Martin PJ, Jih F.** Neural control of heart rate: a conciliation of models. *IEEE Trans Biomed Eng* 23: 164–166, 1976.

23. **Kawada T, Uemura K, Kashihara K, Kamiya A, Sugimachi M, Sunagawa K.** A derivative-sigmoidal model reproduces operating point-dependent baroreflex neural arc transfer characteristics. *Am J Physiol Heart Circ Physiol* 286: H2272–H2279, 2004.

24. **Kawada T, Zheng C, Yanagiya Y, Uemura K, Miyamoto T, Inagaki M, Shishido T, Sugimachi M, Sunagawa K.** High-cut characteristics of the baroreflex neural arc preserve baroreflex gain against pulsatile pressure. *Am J Physiol Heart Circ Physiol* 282: H1149–H1156, 2002.

25. **Kendziorski CM, Cowley AW Jr, Greene AS, Salgado HC, Jacob HJ, Tonellato PJ.** Mapping baroreceptor function to genome: a mathematical modeling approach. *Genetics* 160: 1687–1695, 2002.

26. **King AL.** Pressure-volume relation for cylindrical tubes with elastomeric walls: the human aorta. *J Appl Physics* 17: 501–505, 1946.

27. **Langewouters GJ, Wesseling KH, Goedhard WJ.** The static elastic properties of 45 human thoracic and 20 abdominal aortas in vitro and the parameters of a new model. *J Biomech* 17: 425–435, 1984.

28. **Levy MN, Yang T, Wallick DW.** Assessment of beat-by-beat control of heart rate by the autonomic nervous system: molecular biology technique are necessary, but not sufficient. *J Cardiovasc Electrophysiol* 4: 183–193, 1993.

29. **Levy MN, Zieske H.** Autonomic control of cardiac pacemaker activity and atrioventricular transmission. *J Appl Physiol* 27: 465–470, 1969.

30. **Lu K, Clark JW Jr, Ghorbel FH, Ware DL, Bidani A.** A human cardiopulmonary system model applied to the analysis of the Valsalva maneuver. *Am J Physiol Heart Circ Physiol* 281: H2661–H2679, 2001.

31. **Mark AL.** Sympathetic neural contribution to salt-induced hypertension in Dahl rats. *Hypertension* 17, *Suppl*: I86–I90, 1991.

32. **Melchior FM, Srinivasan RS, Charles JB.** Mathematical modeling of human cardiovascular system for simulation of orthostatic response. *Am J Physiol Heart Circ Physiol* 262: H1920–H1933, 1992.

33. **Miyajima E, Buñag RD.** Exacerbation of central baroreflex impairment in Dahl rats by high-salt diets. *Am J Physiol Heart Circ Physiol* 252: H402–H409, 1987.

34. **Mokrane A, LeBlanc AR, Nadeau R.** Transfer function analysis of vagal control of heart rate during synchronized vagal stimulation. *Am J Physiol Heart Circ Physiol* 269: H1931–H1940, 1995.

35. **Mokrane A, Nadeau R.** Dynamics of heart rate response to sympathetic nerve stimulation. *Am J Physiol Heart Circ Physiol* 275: H995–H1001, 1998.

36. **Moreno C, Kaldunski ML, Wang T, Roman RJ, Greene AS, Lazar J, Jacob HJ, Cowley AW Jr.** Multiple blood pressure loci on rat chromosome 13 attenuate development of hypertension in the Dahl S hypertensive rat. *Physiol Genomics* 31: 228–235, 2007.

37. **Morgan DA, DiBona GF, Mark AL.** Effects of interstrain renal transplantation on NaCl-induced hypertension in Dahl rats. *Hypertension* 15: 436–442, 1990.

38. **Munch PA, Andresen MC, Brown AM.** Rapid resetting of aortic baroreceptors in vitro. *Am J Physiol Heart Circ Physiol* 244: H672–H680, 1983.

39. **Nylander E, Sigvardsson K, Kilbom A.** Training-induced bradycardia and intrinsic heart rate in rats. *Eur J Appl Physiol Occup Physiol* 48: 189–199, 1982.

40. **Olufsen MS, Tran HT, Ottesen JT, Research Experiences for Undergraduates Program, Lipsitz LA, Novak V.** Modeling baroreflex regulation of heart rate during orthostatic stress. *Am J Physiol Regul Integr Comp Physiol* 291: R1355–R1368, 2006.

41. **Petiot E, Barrès C, Chapuis B, Julien C.** Frequency response of renal sympathetic nervous activity to aortic depressor nerve stimulation in the anaesthetized rat. *J Physiol* 537: 949–959, 2001.

42. **Pickering AE, Simms AE, Paton JF.** Dominant role of aortic baroreceptors in the cardiac baroreflex of the rat in situ. *Auton Neurosci* 142: 32–39, 2008.

43. **Rapp JP.** Dahl salt-susceptible and salt-resistant rats. *A review Hypertension* 6: 753–763, 1982.

44. **Rapp JP.** Genetic analysis of inherited hypertension in the rat. *Physiol Rev* 80: 135–172, 2000.

45. **Rogers RF, Rybak IA, Schwaber JS.** Computational modeling of the baroreflex arc: nucleus tractus solitarius. *Brain Res Bull* 51: 139–150, 2000.

46. **Rogers RF, Paton JF, Schwaber JS.** NTS neuronal responses to arterial pressure and pressure changes in the rat. *Am J Physiol Regul Integr Comp Physiol* 265: R1355–R1368, 1993.

47. **Rogers RF, Rose WC, Schwaber JS.** Simultaneous encoding of carotid sinus pressure and dP/dt by NTS target neurons of myelinated baroreceptors. *J Neurophysiol* 4: 2644–2660, 1996.

48. **Rosenblueth A, Simeone FA.** The interrelations of vagal and accelerator effects on the cardiac rate. *Am J Physiol* 110: 42–45, 1934.

49. **Sagawa K.** Concerning "gain". *Am J Physiol Heart Circ Physiol* 235: H117, 1978.

50. **Seagard JL, van Brederode JF, Dean C, Hopp FA, Gallenberg LA, Kampine JP.** Firing characteristics of single-fiber carotid sinus baroreceptors. *Circ Res* 66: 1499–1509, 1990.

51. **Shields RW Jr.** Functional anatomy of the autonomic nervous system. *J Clin Neurophysiol* 10: 2–13, 1993.

52. **Simms AE, Paton JF, Pickering AE.** Hierarchical recruitment of the sympathetic and parasympathetic limbs of the baroreflex in normotensive and spontaneously hypertensive rats. *J Physiol* 579: 473–486, 2007.

53. **Spyer KM.** The central nervous organization of reflex circulatory control. In: *Central Regulation of Autonomic Functions*. New York: Oxford University Press, 1990, p. 168–188.

54. **Srinivasan R, Nudelman HB.** Modeling the carotid sinus baroreceptor. *Biophys J* 12: 1171–1182, 1972.

55. **Srinivasan R, Nudelman H.** Theoretical studies on the behavior of carotid sinus baroreceptors. *Kybernetik* 13: 144–150, 1973.

56. **Taher MF, Cecchini AB, Allen MA, Gobran SR, Gorman RC, Guthrie BL, Lingenfelter KA, Rabbany SY, Rolchigo PM, Melbin J, Noordergraaf A.** Baroreceptor responses derived from a fundamental concept. *Ann Biomed Eng* 16: 429–443, 1988.

57. **Thorén P, Saum WR, Brown AM.** Characteristics of rat aortic baroreceptors with nonmedullated afferent nerve fibers. *Circ Res* 40: 231–237, 1977.

58. **Warner HR, Cox A.** A mathematical model of heart rate control by sympathetic and vagus efferent information. *J Appl Physiol* 17: 349–355, 1962.

59. **Warner HR, Russell RO Jr.** Effect of combined sympathetic and vagal stimulation on heart rate in the dog. *Circ Res* 24: 567–573, 1969.

60. **Wesseling KH, Settels JJ.** Circulatory model of baro- and cardiopulmonary reflexes. In: *Blood Pressure Heart Rate and Variability: Computer Analysis, Methodology and Clinical Applications*, edited by Di Rienzo M, Mancia G, Parati G, Pedotti A, Zanchetti A. Amsterdam: IOS, 1992, p. 56–67.

61. **Whitescarver SA, Ott CE, Kotchen TA.** Parasympathetic impairment of baroreflex control of heart rate in Dahl S rats. *Am J Physiol Regul Integr Comp Physiol* 259: R76–R83, 1990.